Dissertation
submitted to the
Combined Faculties for the Natural Sciences and for
Mathematics
of the Ruperto-Carola University of Heidelberg, Germany
for the degree of
Doctor of Natural Sciences

presented by

Dipl.-Phys. Andrea Borch
born in: Berlin
Oral examination: July 22, 2004

Evolution of the Stellar Mass Density
of Galaxies Since Redshift 1.0

Referees: Prof. Dr. Klaus Meisenheimer
                Prof. Dr. Immo Appenzeller

Entwicklung der stellaren Massendichte von Galaxien seit Rotverschiebung 1.0

Im Unterschied zu anderen Methoden der Massenbestimmung von Galaxien können stellare Massen auch bei höheren Rotverschiebungen und der sich damit ergebenden eingeschränkten Winkelauflösung bei Beobachtung mit bodengebundenen Instrumenten abgeschätzt werden. Für eine Stichprobe von 25000 Galaxien aus der COMBO-17 Durchmusterung werden stellare Massen abgeschätzt. Hierzu wird eine Methode verwendet, die auf der COMBO-17 Multifarbenklassifikation basiert. Es wird eine für diesen Zweck geeignete Bibliothek von Galaxienvorlagen entwickelt. Die Klassifikation mithilfe dieser Bibliothek liefert eine Abschätzung der Rotverschiebung und der spektralen Energieverteilung. Die für alle Typen spektraler Energieverteilung aus der Bibliothek bekannten stellaren Masse-Leuchtkraft-Verhältnisse dienen zusammen mit der Flußmessung in einem der COMBO-17 Filter im optischen Bereich zur Abschätzung der stellaren Masse für die Galaxien aus der Stichprobe.

Die so bestimmten stellaren Massen dienen dazu, die stellare Massenfunktion und die integrierte stellare Massendichte im Rotverschiebungsbereich $0 \leq z \leq 1$ zu bestimmen. Als Ergebnis läßt sich ein Anstieg der stellaren Massendichte um den Faktor 1.6 seit Rotverschiebung 1 feststellen. Dieses Resultat ist in guter Übereinstimmung mit den Vorhersagen semianalytischer Modelle der Galaxienentwicklung und -entstehung. Der Vergleich mit einer Integration der Sternentstehungsrate aus dem Madau-Plot über die Rückschauzeit zeigt eine gute Übereinstimmung dieses relativen Massenzuwachses, aber die absoluten Werte sind verglichen mit den in dieser Arbeit bestimmten stellaren Massendichten um den Faktor 4-5 höher.

Evolution of the Stellar Mass Density of Galaxies Since Redshift 1.0

At variance to other methods of mass estimation of galaxies, stellar masses can be estimated also at higher redshifts and therefore with reduced angular resolutions, when observing with ground based instruments. For a sample of 25000 galaxies drawn from the COMBO-17 survey stellar masses are estimated. For this purpose a method is used that is based on the COMBO-17 multi-color classification. A library suitable for this purpose is developed, and the classification with this library delivers an estimation of the redshift and the spectral energy distribution. The stellar mass-to-light ratio, that is known from the library for all types of spectral energy distribution, together with the flux measurement in one of the COMBO-17 filters in the optical regime delivers an estimation of the stellar mass for the galaxies in the survey.

The stellar masses estimated in this way are used for an estimation of the stellar mass function and of the integrated stellar mass density in the redshift regime $0 \leq z \leq 1$. Resulting from this an increase of the stellar mass density by a factor of 1.6 since redshift 1 is determined. This result is in good agreement to predictions of semianalytic models of galaxy formation and evolution. The comparison to an integration of the star formation rate from the Madau plot over the lookback time shows a good agreement to this relative mass increase but the absolute values are 4-5 times higher than the mass density determined in this work.

Contents

Chapter 1

Introduction

1.1   Galaxy evolution

In the current cosmological picture the universe expanded and cooled after the Big Bang. It was first radiation dominated, until the electrons combined with the protons to form hydrogen and radiation decoupled from the matter. Before the epoch of combination acoustic waves in the radiation dominated plasma were damped (Silk-damping). The Silk-damping refers to baryonic matter, which interacts with radiation. Whereas in dark matter there is no Silk-damping, the free streaming of neutrinos would damp out small-scale density perturbations. The growth of the density fluctuations in the dark matter is not influenced, if the velocity of dark matter particles is small compared to the velocity of light. In this case it is called cold dark matter. Already at the time of combination the density fluctuations were formed, which can be verified as temperature differences of the order of 10^{-5} of the mean temperature observed in the cosmic microwave background with the WMAP satellite.

Galaxies were formed from the growth of primordial density fluctuations of dark matter. These density fluctuations decoupled from the general expansion of the universe and collapsed as soon as the local density was above the critical density. Models of galaxy formation and evolution assume that galaxies were formed firstly as small objects by these density fluctuations mentioned above. They grew into larger and larger objects by merger events. This is the so-called hierarchical picture.

The baryonic matter follows the gravitational potential which is given by the distribution of the dark matter. The dark matter and the baryonic matter interact only by gravitation. The processes when baryonic matter falls into the gravitational potentials of the dark matter are complicated. Here is a short description of them:

Cooling of gas: The baryonic gas will be shock heated when it falls into the dark matter halos. The pressure prevents further contraction. Radiation cooling is the dominating effect that causes finally a Kelvin-Helmholtz contraction [Rees & Ostriker 1977].

Star formation: The cooled gas settles in a disk due to the conservation of angular momentum and forms stars.

Supernova Feedback: After the formation of the first massive stars supernova events bring
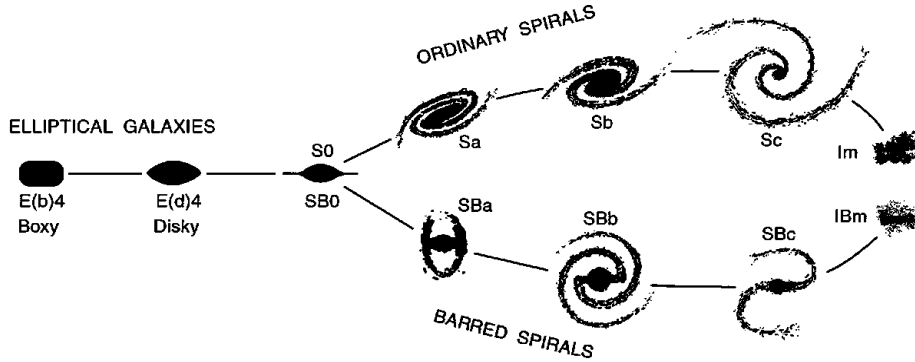
Figure 1.1: The tuning fork diagram from E. Hubble. Taken from Kormendy & Bender 1996

energy into the gas and heat it again. Depending on the depth of the potential well the total gas of a galaxy may be expelled [Dekel & Silk 1986].

Mergers: Two approaching galaxies may merge with each other due to the gravitational inter-action. Such merger events can be demonstrated in computer simulations, for example the antennae galaxy NGC 4038/4039 by [Toomre & Toomre 1972].

Models of galaxy formation and evolution have to take into account the growth of density fluctuations, their mergers with each other and the processes due to the gravitational interaction between baryonic and dark matter. Examples for such models are the so-called semianalytic models [Somerville & Primack 1999, Cole et al. 2000]. In these models Monte Carlo simulations of different merging histories (so-called merger trees) are investigated. The processes due to the interaction effects of the dark matter with the baryonic matter as mentioned above are taken into account as additional assumptions [Somerville & Primack 1999].

1.2   Galaxy types

Different galaxy types vary in their morphology and their color. The morphological types are summarized in the tuning fork diagram following to Hubble (see figure 1.1). Among these there are elliptical and lenticular galaxies. They consist of very old stars (some 10^9 years) and have barely gas and dust and are therefore not able to build new stars. Furthermore there are disk galaxies which consist of a bulge and a disk component. There are old stars in the bulge, whereas the disk harbours young stars. The disk contains gas which can be converted into new stars. Disk galaxies possess a bluer color due to their younger stellar population. Elliptical and lenticular galaxies are called early types whereas spiral galaxies are called late types. Other galaxy types are starburst galaxies. Their colors are dominated by luminous young stars, therefore they are blue. Morphologically they often have a irregular shape.

The morphological classification only makes sense if the galaxies can be spatially resolved, for example in the case of nearby galaxies at low redshifts. At higher redshifts this is hardly possible with ground based telescopes due to the seeing limited resolution. Only integral properties such as the color or the spectrum of the galaxy can be measured. In those cases a classification into different types of spectral energy distribution (SED) is useful, which is also used in this work.

1.3 Luminosity function

Large and deep samples of galaxies enable statistical investigations of the properties of the population of galaxies with redshift and therefore with lookback time. One important property of galaxies is their absolute luminosity. The luminosity function describes the frequency distribution of galaxies as a function of their luminosity. Figure 1.2 shows the local luminosity function of galaxies of different Hubble types. The elliptical galaxies are most luminous and the irregulars are the faintest.

Galaxies are not uniformly distributed but form groups, clusters and superclusters which are found in filaments and wall-like structure in the universe. This large scale structure also contains large voids containing almost no galaxies. Galaxies which are not part of a cluster are called field galaxies. Field galaxies are investigated in this work. In figure 1.2 the luminosity function of field galaxies is compared to those in the Virgo cluster. Noticeable the cluster galaxies show a different distribution to the galaxies in the field, because the evolution depends on properties of the environment (e.g. galaxy density, density of the intergalactic gas).

1.4 Surveys

The evolution of the luminosity function was and is investigated with different surveys. It is important to have a sample of galaxies as big as possible because of two reasons:

- The sample should be divided in various subgroups, which distinguish different features of each other. For example it is useful to distinguish different redshift intervals, different luminosity intervals or different galaxy types.

- Each of these subgroups of different features should contain a sufficient number of objects in order to keep the error of the Poisson-statistics small.

Because of the large scale structure mentioned above it is also important to investigate a representative volume. This can be achieved by involving a large area on the sky which covers typical length scales of large scale structure features or taking many independent fields into account.

The Canada-France Redshift Survey (CFRS) [Lilly et al. 1995] investigated 591 I-band selected galaxies ($I < 22.0$) in the redshift regime $0.05 < z < 1$. The Calar Alto Deep Imaging Survey (CADIS) [Fried et al. 2001] examined a sample of 2779 galaxies with $I_{815} < 23.0$ in the regime $0.3 < z < 1.0$. As a follow-up project of CADIS the COMBO-17 survey (Classifying Objects by Medium Band Observations in 17 filters) investigated the luminosity function for a sample of 25000 galaxies with $R < 24$ in the regime $0.2 < z < 1.2$ [Wolf et al. 2003].

The COMBO-17 survey is also used as the groundwork of this thesis. It is a multi-color survey, which has been taken in 5 broad band and 12 medium band filters. It was taken with the Wide Field Imager at the 2.2m telescope on La Silla. Currently there are 3 fields completely analysed available, which cover together an area of 0.8 square degree on the sky. Two further fields, which will extend the COMBO-17 survey to 6 fields in total corresponding to an area of 1.5 square degree, are in preparation. A multi-color classification delivers both an estimation of the redshift and the SED type. This is described in detail in section 2.1.
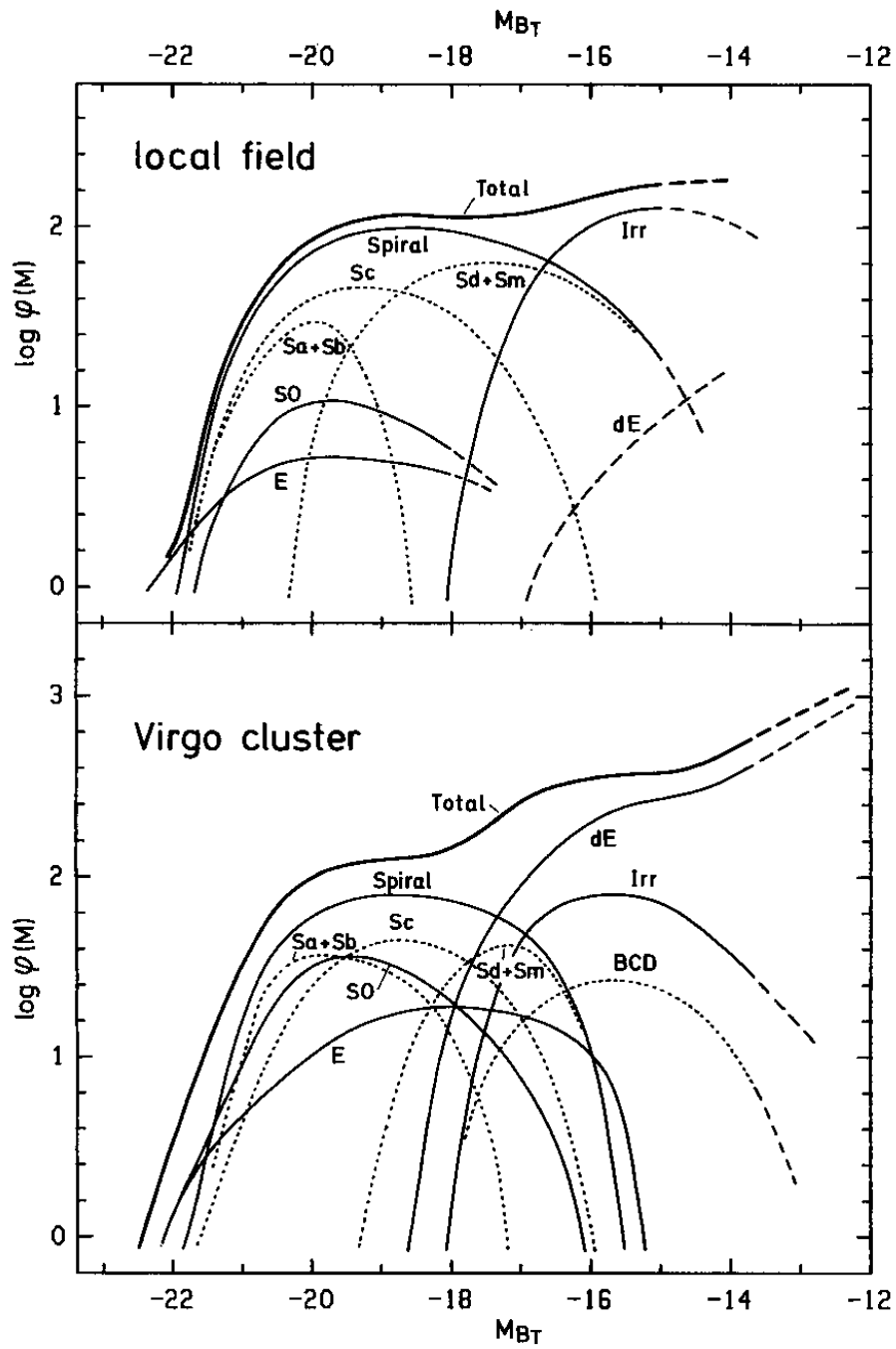
Figure 1.2: The luminosity function of different galaxy types in the field and in the Virgo cluster. (Figure 1 from [Binggeli et al. 1988]). The luminosity function $\varphi(M)$ is plotted against the absolute B-band luminosity.

With the aid of the GEMS survey (Galaxy Evolution with Morphologies and SED's, [Rix et al. 2004]) also the morphological information is available. In this project one COMBO-17 field is observed with the Advanced Camera for Surveys of the Hubble Space Telescope. Compared to ground based imaging a considerably higher resolution is achieved. Therefore for more distant objects morphological information such as the effective radius, spiral structure or occurring merger events can be determined.

1.5   Mass estimation

The mass of a galaxy can be determined by its dynamical properties. The dynamical properties differ for various galaxy types:

- Disk galaxies show a rotation along their symmetry axis.

- Elliptical galaxies show no or only slow rotation. The orbits of their stars have mostly a statistical distribution and can be distributed by a velocity dispersion.

For disk galaxies rotation curves can be determined by measuring rotational velocities in dependence of the distance to the galactic center, for example by measuring the Doppler shift of spectral lines. Assuming a Kepler rotation the mass of the galaxy can be estimated. For slow or non-rotators such as elliptical galaxies this is not possible. Their masses can be estimated by using the virial theorem. It can be applied to systems which are in dynamical equilibrium due to the influence of gravitation. In such systems the kinetic energy is half of the potential energy and can be estimated by using the velocity dispersion.

Both methods deliver the total masses including the dark matter within the investigated radius. The stellar mass of a galaxy can also be estimated by using its stellar mass-to-light ratio. The integrated luminosity is a measure for the stellar mass, because the light that comes from a galaxy is dominated by its stellar component. This method is thus applicable even for very distant objects which cannot be resolved.

A main problem of the use of luminosities for stellar mass estimation is the fact that young stars are brighter than average at shorter wavelength. The reason is that young stellar populations contain massive stars which have a comparatively short lifetime and a high surface temperature. The luminosity of stars is proportional to T^4, so hot stars are very bright and dominate the spectrum although they are rare objects. Due to the Wien's displacement law this is in particular important in the short wavelength regime. Luminosities at wavelengths below the 4000 Å break can therefore cause errors in the stellar mass estimation. The stellar masses are mostly dominated by old stars, which have negligible luminosities compared to the young stars. In order to avoid such problems, infrared luminosities such as the K band luminosity are proposed as a proxy for the stellar mass [Broadhurst et al. 1992, Kauffmann & Charlot 1998]. The K-band luminosities measure predominantly low mass stars, which are more frequently.

A first approach to determine the stellar mass, the luminosities of galaxies are therefore measured in the infrared regime. Some surveys measure the K-band luminosity function. Examples are the MUNICS survey [Drory et al. 2003], the K20 survey [Pozzenti et al. 2003], and the 2MASS survey [Kochanek et al. 2001]. Whereas Kochanek et al. assume a unique M/L ratio for all galaxy types in order to transform the K-band luminosities into stellar masses, the

objects in the MUNICS survey are classified with a multi-color classification. For this purpose a template library on the basis of stellar population synthesis models is used, similar to the method presented in this work. Whereas in the infrared regime the K-corrections are similar for different galaxy types, they cover a larger range in the optical regime [Lilly et al. 1995]. The K-corrections are in order to "correct" the apparent magnitudes of distant galaxies for the effects of redshifting their spectra which are observed through filters with a fixed central wavelength.

A different method of estimating the stellar M/L ratios is done by Kauffmann et al. [2003]. They use the strength of the 4000Å break (measured as D4000 parameter) together with the equivalent width of the Balmer absorption line Hδ in order to draw a direct correlation of the (D4000,$H\delta$) parameter space to the M/L ratios. This relation is applied to 10^5 galaxies in the Sloan Digital Sky Survey (SDSS).

The K-band luminosities have some uncertainties which are caused by stars at the asymptotic giant branch (AGB). Although these stars are very rare they may dominate the near infrared luminosities. In the age regime between 100 Myr and about 3 Gyr the thermal-pulsating AGB stars alter the K-band mass-to-light ratio by a factor of up to 0.3 dex [Mouhcine & Lançon 2003]. As described in section 2.3, these stars are difficult to model.

In the method described in this work the stellar masses are estimated by using optical luminosities and therefore the disadvantages of the K-band luminosities are avoided. The same is the case for the aforementioned method of Kauffmannn et al. [2003] who use the luminosities in the z-band.

1.6   Science objectives

In section 1.1 the semianalytic models of galaxy formation in the context of the contemporary standard model are mentioned. In order to test these models they are compared to observational results of surveys. In the past the luminosity function was available for this. For this purpose the primary model predictions of galaxy masses have to be transformed into luminosities.

A more direct test of such models would be the integrated stellar mass density in galaxies and its evolution with redshift. The method of mass estimation presented in this work enables to estimate the integrated stellar mass density in the redshift regime $0.1 < z < 1.0$ by using a sample of 25000 galaxies drawn from the COMBO-17 survey. This is compared to predictions of semianalytic models. The method of stellar mass estimation is presented in chapter 3. It is based on a library of galaxy spectra, which is introduced in chapter 2. The comparison to the semianalytic models is shown in chapter 3.4, where the results are presented.

Furthermore it is interesting to compare the integrated stellar mass density to a integration of the Madau plot [Madau et al. 1996]. The Madau plot (figure 1.3) shows the integrated star formation rate in dependence of the redshift. If the star formation rate is integrated over the lookback time, one should expect the integrated stellar mass density in galaxies. This can be compared to the result of this work. The comparison is done in chapter 5. Since the SFR in the Madau plot measures rather the massive stars, such an investigation allows to compare a star formation rate which is dominated by high mass stars to a star formation rate of typical solar
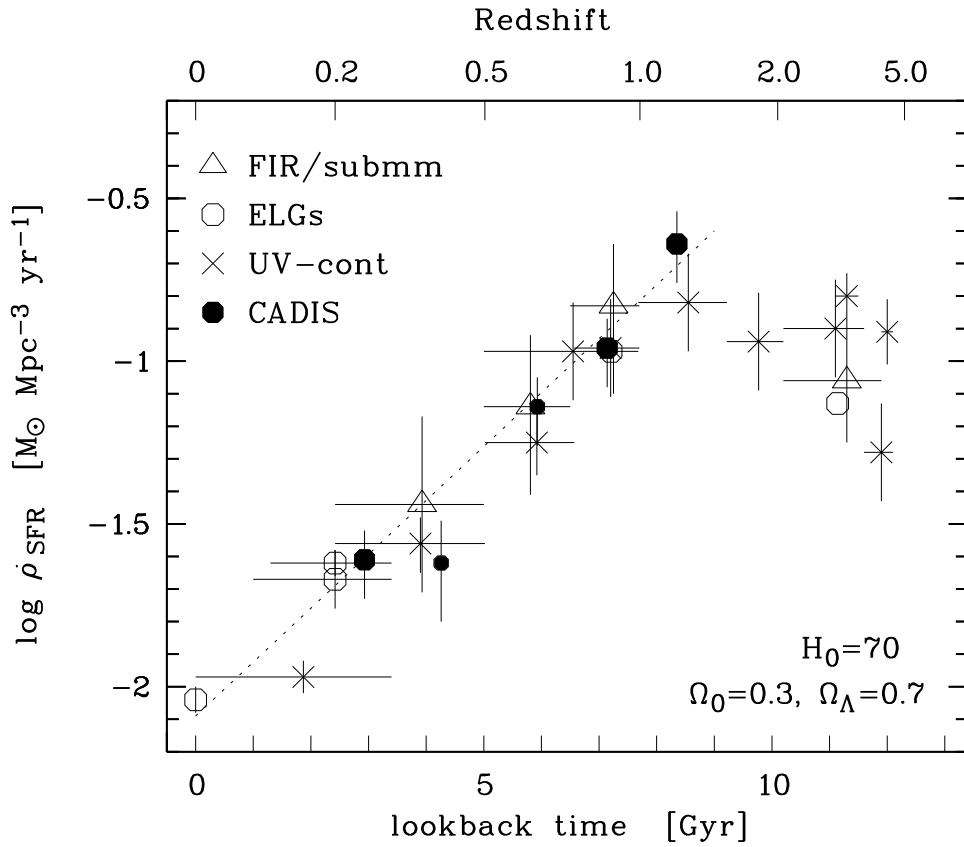
Figure 1.3: The integrated star formation rate in galaxies (Figure 12 from [Hippelein et al. 2003]). The y-axis shows the star formation rate per comoving volume as a function of redshift. At the x-axis the redshifts are translated to lookback times by using the standard cosmology. The dashed line is a "by hand" fit to the data [Hippelein et al. 2003].

mass stars. Discrepancies between the Madau plot and the stellar mass result since redshift 1.0 would imply important consequences, which are discussed in chapter 5.

Chapter 2

The galaxy template library

2.1 Multi-color-classification of galaxies in COMBO-17

COMBO-17 is a multi-color survey. It covers four different fields with a total area of one square degree on the sky. Currently three fields are available for the analysis: A field around the Chandra Deep Field South (CDFS), a field containing the Abell 901 cluster (A901) and an equatorial field (S11). The observations are taken in 5 broad band filters and 12 medium band filters (Figure 2.1). The filter set is tailored for covering the whole optical wavelength range.

The object classification in COMBO-17 relies only on the colors determined from this filterset. No additional morphological information is used. The colors of the objects in the surveyed sample are compared to color libraries of different object classes. First, it is distinguished between 4 different classes of objects:

- main sequence stars

- white dwarfs

- galaxies

- quasars

Each library is designed in such a way that the colors of all the library members are representative for the considered object class. This enables us to assign 99.7 % of all survey objects to one of these four classes.
The objects are not only associated with different classes but also distinguished between different types among each class. The different types in each class are called SED (spectral energy distribution) types. This leads to an estimation of the SED parameter for each class and in addition, for the galaxy and quasar class the redshift has to be taken into account.

The classification process works as follows: The colors of each survey object and their errors are compared to the color distribution of each library object. A probability for the affiliation of a survey object to a certain library object is calculated. For each object class the probability of belonging to it is calculated as the sum over the probabilities of all library members of this class. The object is assigned to the class with the highest probability in cases where the relative probability is greater than 0.75 times the sum of the probabilities in all classes. Otherwise the
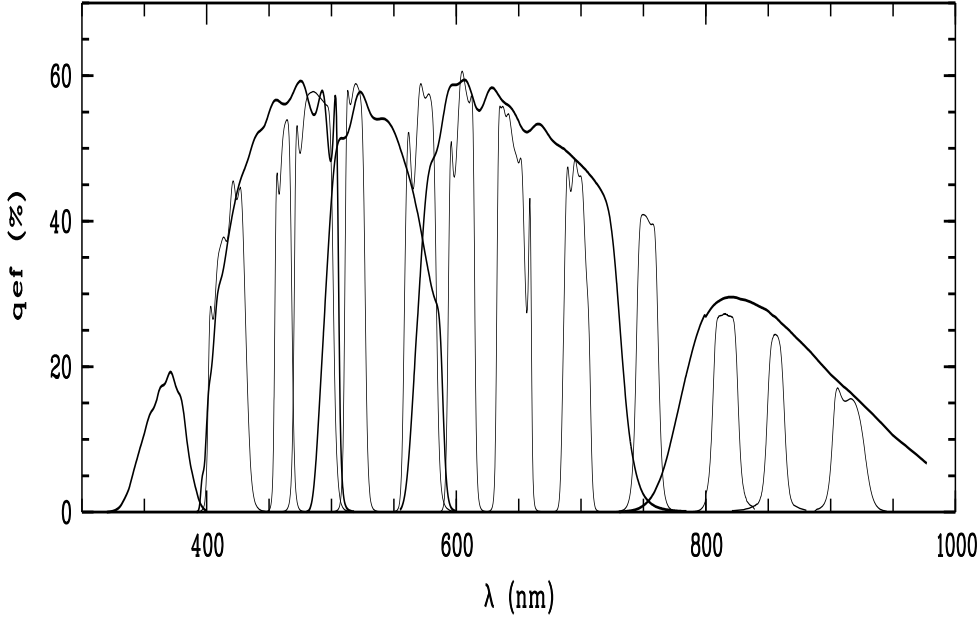
Figure 2.1: The filterset of COMBO-17. The quantum efficiency (qef) of all filters is shown as a function of wavelength. The thick lines are the five broadband filters and the thin lines are the 12 medium band filters.

object is called unclassifiable and cannot be assigned to any class.

The libraries are designed such that they cover the whole color space in the regime of consideration. This allows to define a distance of the considered survey object to the nearest library object. If this distance exceeds a value of 3σ, where σ is the gaussian variance, the object is called peculiar [Wolf, PhD thesis, Wolf et al. 2004].

The multi-color classification is described in more detail in [Wolf et al. 2001b, Wolf et al. 2004].

The stellar library has been built from the Pickles atlas and the white dwarfs from the synthetic library of Koester (see [Wolf et al. 2004] and references therein). The quasar library is built from SDSS QSO template spectra [Wolf et al. 2003b]. For the galaxy class there are three different libraries available. The first library is the Kinney et al. library [Kinney et al. 1996] which has been used in COMBO-17 [Wolf et al. 2001b]. It is used for the classification in [Wolf et al. 2003], who investigated the evolution of the galaxy luminosity function in COMBO-17. Another library is developed in this thesis. A third library is developed by C. Wolf [Wolf et al. 2004] which is currently used in COMBO-17. These three libraries can be used alternatively. The differences between them will be discussed later.

The Kinney et al. library is based on averaged UV-optical spectra of nearby galaxies of Kinney et al. [1996] which cover the wavelength range between 120 nm and 1000 nm. These spectra are obtained with an aperture of 200 square arcseconds in order to match the ground based optical spectra to the aperture of the UV spectra obtained with the IUE satellite [Kinney et al. 1996]. Hence, these spectra sample only the inner region of the galaxies. This property is good for our

purpose since the outer regions of the galaxies are often too faint to be observed, in particular for high-redshift galaxies. The Kinney-spectra contain 10 different morphologically classified Hubble types. There are the four galaxy types elliptical, lenticular, Sa, and Sb. In addition there are six types of starburst galaxies SB6 to SB1. In order to create a color library for COMBO-17 these 10 galaxy types are interpolated to 100 SED types in color space. These 100 SED's are shifted to different redshifts, again in color space. As a result a library of 47000 objects is obtained, consisting of 100 SED types times 470 redshifts in the range between 0.0 and 1.5. The spacing between the redshifts is equidistant on a log(1+z) scale. The redshift range is chosen greater than the highest measurable redshift where 2 filters bracketing the 4000 Å break (z=1.2 for the currently used filterset) in order to avoid boundary effects.

2.2 The aims of a new library

The Kinney et al. library described in the last section has been used for classification at the time when I started this work. The classification with this library was still used for the investigation of the luminosity function [Wolf et al. 2003]. The main disadvantage of this library is that the estimation of the SED parameter is hard to interprete in terms of astrophysical meaning, because there is no other information than the colors available.

This work aims at estimating the stellar masses of galaxies. For this purpose one needs to transform the luminosities to stellar masses by using a stellar mass-to-light ratio. In order to determine the stellar mass-to-light ratio by using the SED estimation, it is necessary to assign a stellar mass-to-light ratio to each SED type. Stellar mass-to-light ratios can be determined for a given star formation history by using stellar population synthesis codes. One of these codes is described in the next section. In order to link a star formation history to a given SED type a new library that contains this information is necessary.

This library needs to be suitable for multi-color classification in COMBO-17 and needs to deliver reliable SED and redshift estimation. Going in the direction towards a new library two steps are done: Firstly, synthetic spectra of the stellar population synthesis are matched to the spectra of the Kinney et al. library, because this library is proven to be suitable for multi-color classification. This step is shown in section 2.4. In a second step these fits in order to create a new library for classification in COMBO-17, as shown in section 2.5.

The new library has to be proven to deliver SED and redshift estimation as reliable as the Kinney et al. library or better, when using it for multi-color classification in COMBO-17. The comparison of the libraries is shown in section 2.6. The former Kinney et al. library is replaced by this new library in the multi-color classification process. As mentioned above, this new library should be better suited for the stellar mass estimation.

2.3 The stellar population synthesis code PEGASE

Stellar population synthesis models are based on the assumption that the spectrum of a galaxy is assembled by the spectra of many stars in this galaxy. For nearby galaxies contemporary instruments allow high-quality imaging, so that these galaxies can be studied in detail. In the case of high-redshift-galaxies only the average spectrum built of the whole galaxy is available. In

order to understand such averaged spectra one needs some kind of modeling, where the assembly of all the stars is reconstructed. The averaged spectrum is subsequently built by summing-up the stellar spectra.

For that purpose during the last few decades several so-called stellar population synthesis codes were developed. It started historically with the galaxy evolution program of B.M. Tinsley [Tinsley 1972], who modeled the evolution of stars followed from the main sequence to the beginning of the AGB phase by using semi-empirical tracks and calculated galaxy properties like colors and M/L ratios in timesteps of 1 Gyr. In the following time other stellar population models were published. Examples are the "model of spectroscopic evolution" [Guiderdoni & Rocca-Volmerange 1987], the "isochrone synthesis" [Bruzual & Charlot 1993] and the "Projet d'Etude des GAlaxies par Synthese Evolutive" (PEGASE) [Fioc & Rocca-Volmerange 1997].

In principle stellar population models follow a given law of the star formation history and produce new stars by obeying this law with a mass distribution given by an initial mass function (IMF). Usually such models consist of two different parts. One part contains evolutionary tracks describing how stars evolve in the Hertzsprung-Russel diagram. Models of stellar evolution are used to determine the tracks in the Hertzsprung-Russel-diagram for a grid of stars with different masses and metallicities. The second part contains stellar libraries describing how stars on a given position in the Hertzsprung-Russel-diagram look like. Models of stellar atmospheres are used to determine for a grid of stars with different temperatures, metallicities and surface gravities the spectra of these stars. Since modeling spectra of stellar atmospheres with a sufficient resolution is difficult and expensive in computational time, often measured stellar libraries are used. However, some regions in parameter space (e.g. very low metallicities) are hard to observe and therefore synthetic stellar libraries are needed. Both parts are linked together by stellar population synthesis codes. The stars follow the evolutionary tracks and populate the galaxy respective to their evolutionary velocity along the tracks. The spectra of all stars belonging to the population are summed up to a integrated spectrum.

Whereas the code of Bruzual and Charlot [Bruzual & Charlot 1993] and the PEGASE code agree in the visible, PEGASE aims in particular at an extension to the near infrared regime and link it continuously to the visible, so that the entire wavelength range between 22 nm and 5μm is covered. The near infrared regime is particularly interesting for studies of galaxy evolution, because it is less dominated by young stars, when comparing to the UV-optical regime. Hence it allows investigations of the underlying old stellar population. Keeping in mind the future extension of COMBO-17 to the infrared by the OMEGA 2000 instrument this was the reason for the choice of the PEGASE code.
The spectral region around 1μm is difficult to model, because of the poor knowledge of the atmospheres of cold stars, and also because of rapid evolutions of red supergiants and AGB stars. The PEGASE code with its matching of measured infrared colors seemed to be the best approach at the time when I started this work. However, in 2003 Bruzual and Charlot made a version of their code available [Bruzual & Charlot 2003] that includes spectra of C-type thermal pulsating AGB (TP-AGB) stars and TP-AGB evolutionary tracks, which are expected to be better suited to predict the near infrared fluxes. Nevertheless, because the galaxy template library described in the next two sections was already developed at that time I stick to the PEGASE code.

The code allows to tune a considerable number of parameters. The star formation rate can

be chosen as desired. In the next section I will concentrate on an exponential decaying star formation rate which follows the law

$$SFR(t) = SFR(0) \frac{\exp(-t/\tau)}{\tau} \qquad (2.1)$$

and on a constant star formation rate which follows the law

$$
\begin{aligned}
SFR(t) &= SFR(0) \quad if \ t \leq \tau \\
&= 0 \qquad\quad if \ t \geq \tau
\end{aligned}
\qquad (2.2)
$$

The metallicity evolution can be chosen as a constant metallicity or as a consistent metallicity evolution, where the initial metallicity can be selected arbitrary in a wide range. However, the metallicity evolution takes a single gas component into account only. It does not distinguish between different gas phases such as cold gas clouds or the hot intercloud medium. If infall and galactic winds are neglected, the consistent metallicity evolution is practically a closed box model. Hence, there occur issues known for the closed box model such as the "G-dwarf problem" [Pagel 1997].

The extinction is calculated by using the hydrogen column density where the metallicity of the interstellar medium is taken into account. Hence the geometry of the stellar population influences the extinction. For the extinction the code allows several choices, for example no extinction, extinction for a spheroidal geometry and extinction for a disk geometry with different inclination angles.

The output quantities are normalized to $M_{tot} = 1M_\odot$. The output ASCII file of the PEGASE code `spectra` is given in a format where the continuum fluxes and the line energies are given separately. For the following analysis I transform these into spectra that contain both the continuum and the emission lines.

2.4   Fitting of the spectra of nearby galaxies

As mentioned in section 2.2 the stellar population synthesis code described in the last section is used to produce synthetic template spectra of galaxies which fit the Kinney et al. [1996] spectra described in section 2.1. The PEGASE spectra produced in this way are used in section 2.5 to construct a new library, which is also tailored for multi-color classification. The modeling described in this section aims at an astrophysical parametrization of the galaxy spectra that is kept as simple as possible. For the multi-color classification purpose only a few parameters may be constrained by the classification. Therefore, the simplest approaches which deliver suitable template spectra are best suited for this purpose. However, some assumptions are included that are not really constrained by the spectra but rather astrophysically motivated. Since in stellar population models the parameter space is degenerated, at least some assumptions are necessary.

For the star formation history a three-component model is assumed. It is shown in figure 2.2. The first component (B) simulates an initial burst that happened several Gyr ago. It is modeled as an exponential decaying star formation rate, as described in equation (2.1) with a time constant of $\tau = 1$ Gyr. This time constant aims at compromizing the rapid formation

period motivated by the $[\alpha/Fe]$ ratios of elliptical galaxies [Matteucci 2003] and a delayed star formation due to gas infall or feedback. As a second component (A) a constant star formation rate since the initial burst is assumed. This simulates ongoing star formation processes in disk galaxies and also mimics smaller starbursts occurring during the lifetime of the galaxy. The galaxy types (E-Sb) consist only of these two components. For the starburst galaxies a third component (C) is assumed, that simulates a second burst in the recent past (about 60 Myr ago).

A consistent metallicity evolution is assumed for the B- and the C-component. In order to keep the modeling as simple as possible no gas infall is taken into account. The star formation rate for the B-component is tuned in such a way that after 8 Gyr the initial gas is practically exhausted. An example of its evolution is shown in table 2.1.

The initial metallicity in the B-component is considered as a free parameter. For the A-component the metallicity is fixed constant and no extinction is assumed due to its minor contribution to the stellar population. For the extinction of the B-component a spherically symmetry is assumed in order to simulate something like a bulge or the inner region of an elliptical. For the extinction of the C-component there is a disk geometry assumed, which is averaged over all inclination angles, because in COMBO-17 the inclination angle of the objects is unknown. The IMF is taken from Kroupa et al. [1993].

Hence, there are 5 free parameters: The initial metallicity of the B-component, the age of the old stellar populations, the a/b ratio, the c/b ratio and the d parameter. The parameters a, b and c are used for the linear combination of the star formation history (see figure 2.2). The d parameter describes the time since the second burst. The a/b ratio simulates the constant star formation rate compared to the height of the initial burst and the c/b ratio simulates the height of the second burst compared to the height of the initial burst.

This model is suitable to deliver a reasonable fit to the Kinney et al. spectra as described below. It has never been tested that this solution is the best one in the sense that it minimizes the degrees of freedom which are unconstrained by the multi-color classification. In principle there are other possibilities. For example, for the B component it is possible to vary the time constant of the exponential function instead of the age of the stellar population. It may also be possible to find solutions without the A component. For the C component one can also think about a rectangle function instead of an exponential function. For the dust extinction other assumptions may be possible. In the following I aim at keeping the metalliticy fixed and only varying the age parameter. Alternatively, one may think about fixing the age parameter and varying the metallicity parameter.

In order to obtain the parameters for the PEGASE-spectra by matching them to the Kinney et al. spectra the minima of the χ^2-Plots are considered. Usually the χ^2 function is defined as:

$$\chi^2 = \frac{1}{N-1} \sum_i \frac{(X_i - Y_i)^2}{\sigma_i^2}$$

For comparing the PEGASE spectra to the Kinney spectra the errors σ_i are not taken into account because the flux errors of the averaged Kinney et al. spectra are unknown. Instead of the values X_i and Y_i I rather use logarithms because in the classification algorithm colors are
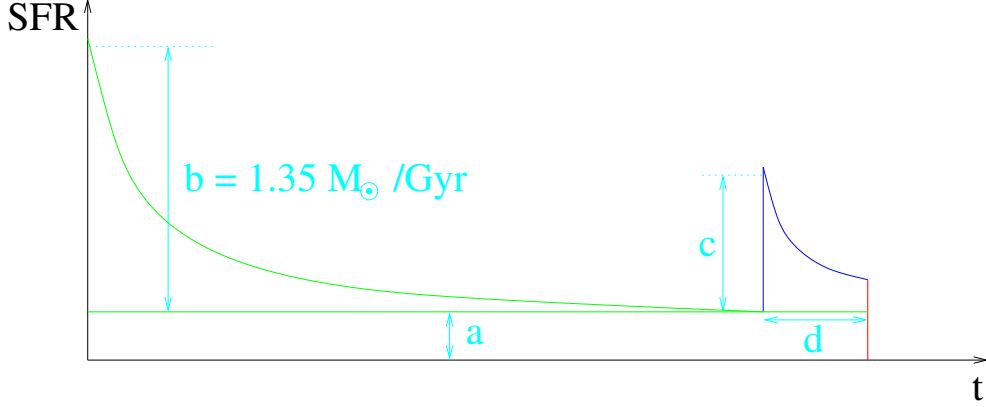
Figure 2.2: The assumed model for the star formation history. The star formation rate is plotted as a function of time. It is composed by three different components which are linear combined by using the factors a, b and c of the respective component.

Table 2.1: Evolution of the gas content and the metallicity of an exponential decaying star formation rate with a time constant of 1 Gyr and an initial value of 1.35 $M_\odot/Myr$. M_{gas} is the mass fraction in the gas component, Z_{ISM} the metallicity of the interstellar medium, and Z_{stars} the mean metallicity of stars.

t/Myr	$M_{gas}/M_\odot$	Z_{ISM}	Z_{stars}
200	0.778	0.007	0.005
400	0.609	0.011	0.007
600	0.476	0.015	0.009
800	0.370	0.018	0.010
1000	0.286	0.022	0.011
2000	0.073	0.039	0.017
3000	0.016	0.051	0.019
4000	0.007	0.049	0.020
5000	0.012	0.046	0.020
10000	0.050	0.036	0.020

used, which are defined as differences of magnitudes, which are defined on a logarithmic scale. Another reason is that they are more sensitive to the lower flux values at the blue end of the spectra. Keeping the purpose of multi-color-classification in mind, we are particularly interested in the blue end of the spectrum, because for example at redshifts about 1, most of the spectrum above the 4000 Å break is shifted outside of the wavelength window. Therefore I use a function that compares the logarithms of the fluxes of the Kinney et al. spectra $F_{\nu,Kinney}$ with the fluxes of the PEGASE spectra $F_{\nu,PEGASE}$. My "χ^2" function is calculated in the following form:

$$\chi^2 = \frac{1}{N} \sum_i \left(\log F_{\nu,Kinney,i} - \log(k \cdot F_{\nu,PEGASE,i}) \right)^2 \tag{2.3}$$

The term $N - 1$ is replaced by N which causes negligible differences for large numbers ($N \geq 1000$). A scaling factor k is included for the following reason:
Since I am only interested in the colors of the spectra, I consider only relative fluxes without any absolute calibration. But for the calculation of the χ^2 function the considered PEGASE spectrum has to be matched to the Kinney spectrum.

This k factor is chosen in such a way, that the derivative

$$\frac{d\chi^2}{dk} = \frac{-2}{k \cdot N} \sum_i \left(\log F_{\nu,Kinney,i} - \log(k \cdot F_{\nu,PEGASE,i}) \right) \tag{2.4}$$

vanishes. At this point there is

$$N \cdot \log k = \sum_i \left(\log F_{\nu,PEGASE,i} - \log F_{\nu,Kinney,i} \right) \tag{2.5}$$

and hence

$$k = 10^{\frac{1}{N} \sum_i \left(\log F_{\nu,Kinney,i} - \log \cdot F_{\nu,PEGASE,i} \right)} \tag{2.6}$$

After calculating the scaling factor the χ^2 function is determined. This is done for a grid of two different parameters for the PEGASE spectra. The χ^2 function is not available in the form of an analytic function of the parameters and has therefore to be calculated numerically for each grid point.

Figure 2.3 shows the χ^2 plots of the parameters age and metallicity for the galaxy types (E-Sb). For the elliptical and lenticular galaxies there are two different minima in the χ^2 plot, a fact that is known in the literature as age-metallicity-degeneracy. Concentrating on solutions with initial metallicities around $Z = 0.001$ (corresponding to about 5% solar metallicity) the ages show a wide distribution between 8 Gyr for Sa galaxies and at least 20 Gyr for E and S0 galaxies. Hence, the ages of elliptical and lenticular galaxies are inconsistent with the age of the universe by using the contemporarly assumed value of the Hubble constant ($H_0 \approx 65$ km/s Mpc). This might reflect a problem of the consistent metallicity evolution in the PEGASE code, which is in this case practically a closed-box model, as mentioned in the last section. However, in this thesis I cannot address these issues but will concentrate on an "empirical" parametrization of the template spectra.

In Figure 2.4 the χ^2 plot of the parameters a/b ratio and metallicity is shown for the Sb and Sa galaxies. Following the results of figure 2.3 the ages are chosen as 10 Gyr for a Sa galaxy
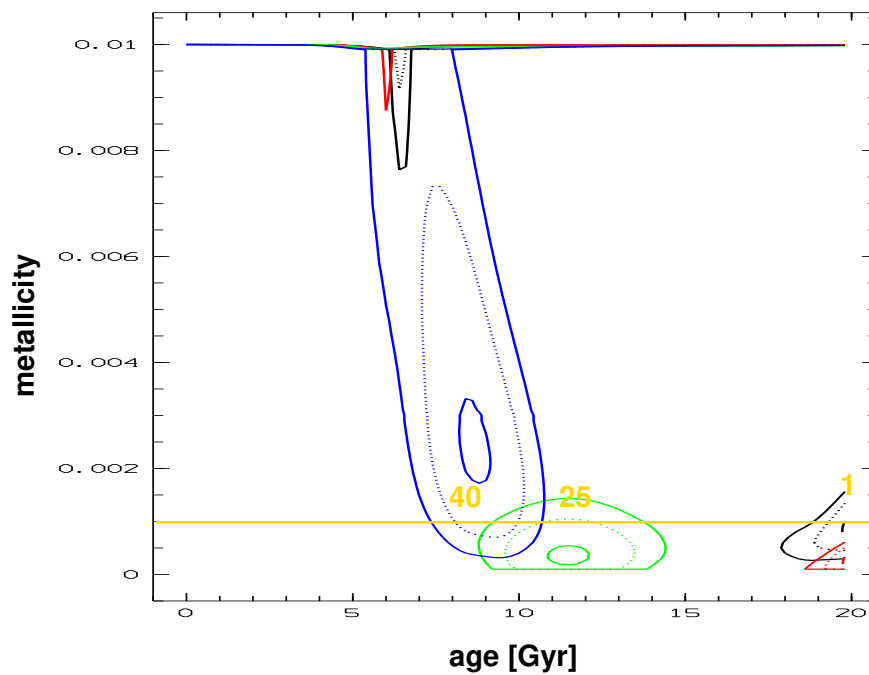
Figure 2.3: χ^2 minima in the plane age vs. metallicity for the galaxy types (E-Sb). The plotted contour levels are 1%, 10% and 20% above the minimal χ^2 value. The colors show the different galaxy types: E in black, S0 in red, Sa in blue and Sb in green. The yellow line shows the metallicity that is chosen for the library described in section 2.9 and the yellow numbers are the SED types.
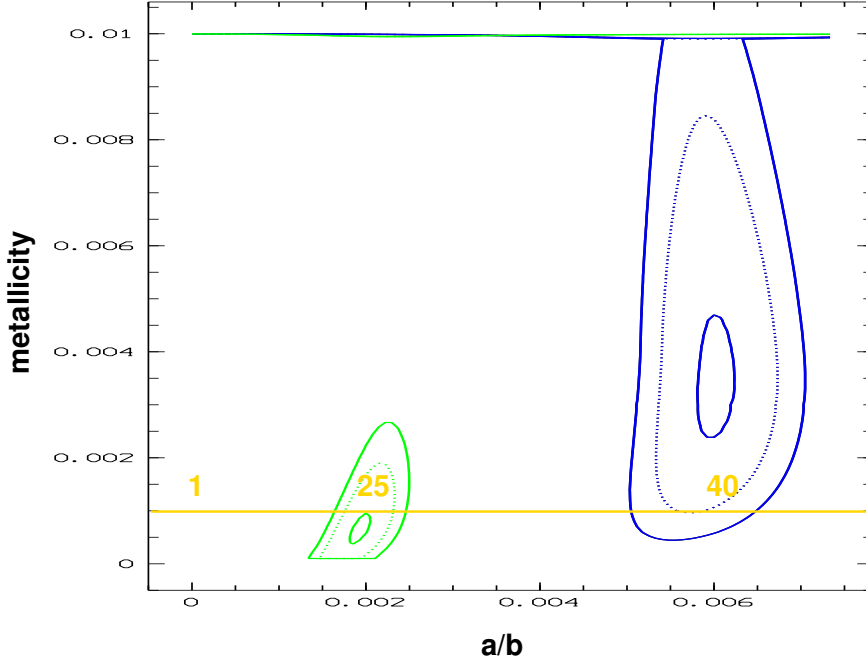
Figure 2.4: χ^2 minima in the plane a/b ratio vs. metallicity for the galaxy types Sa and Sb. The plotted contour levels are 1%, 10% and 20% above the minimal χ^2 value. The colors show the different galaxy types: Sa in blue and Sb in green. The yellow line shows the metallicity that is chosen for the library described in section 2.9 and the yellow numbers are the SED types.

and 8 Gyr for a Sb galaxy. The fits of the initial metallicities are similar to the results from figure 2.4. Therefore, it should be accurate enough to fix the initial metallicity parameter for all (E-Sb) type galaxies to a value of $Z = 0.001$. The a/b ratio delivers best fits at 0.05 for a Sa galaxy and 0.16 for an Sb galaxy.

For starburst galaxies there is an old stellar population together with a second burst, as seen in figure 2.2. In order to keep the modeling as simple as possible the old stellar population is always chosen as the same Sb galaxy with the parameters as mentioned above. The choice of an Sb galaxy for this purpose is taken in order to create a library that is continuous in the parameters, as described in the next section. The fits of the c and d parameters for different Kinney types of starburst galaxies are shown in figure 2.5.

As a summary the parameters derived with this method are shown in table 2.2. The results of the fitted spectra are shown in figure 2.6 for the (E-Sb) type galaxies and in figure 2.7 for the starburst galaxies. Beside the internal extinction of the PEGASE code there is no other (foreground) dust extinction taken into account.
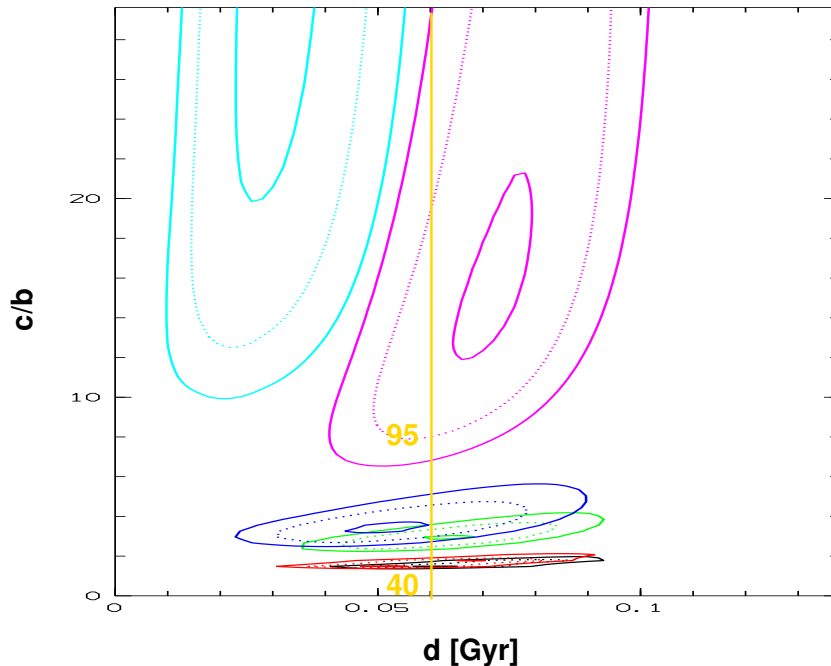
Figure 2.5: χ^2 minima in the plane c/b ratio (y-axis) vs. the time since the second burst d (x-axis) for starburst galaxies. The plotted contour levels are 1%, 10% and 20% above the minimal χ^2 value. The colors show the different galaxy types: SB6 in black, SB5 in red, SB4 in green, SB3 in blue, SB2 in purple and SB1 in light blue. The yellow line shows the metallicity that is chosen for the library described in section 2.9 and the orange numbers are the SED types.

Table 2.2: The parameters for the PEGASE spectra. The parameters are shown in figure 2.2. The age is given for the old stellar population. The a/b is the fraction between the constant star formation rate and the height of the initial burst. c/b is the fraction between the height the second burst and the height of the initial burst.

Type	Age [Gyr]	a/b	c/b	d [Myr]
E	20.0	0.0	0.0	–
S0	20.0	0.0	0.0	–
Sa	11.8	0.0019	0.0	–
Sb	8.6	0.0059	0.0	–
SB6	8.0	0.0059	1.48	60
SB5	8.0	0.0059	1.78	60
SB4	8.0	0.0059	2.96	65
SB3	8.0	0.0059	3.70	50
SB2	8.0	0.0059	16.3	70
SB1	8.0	0.0059	22.2	30
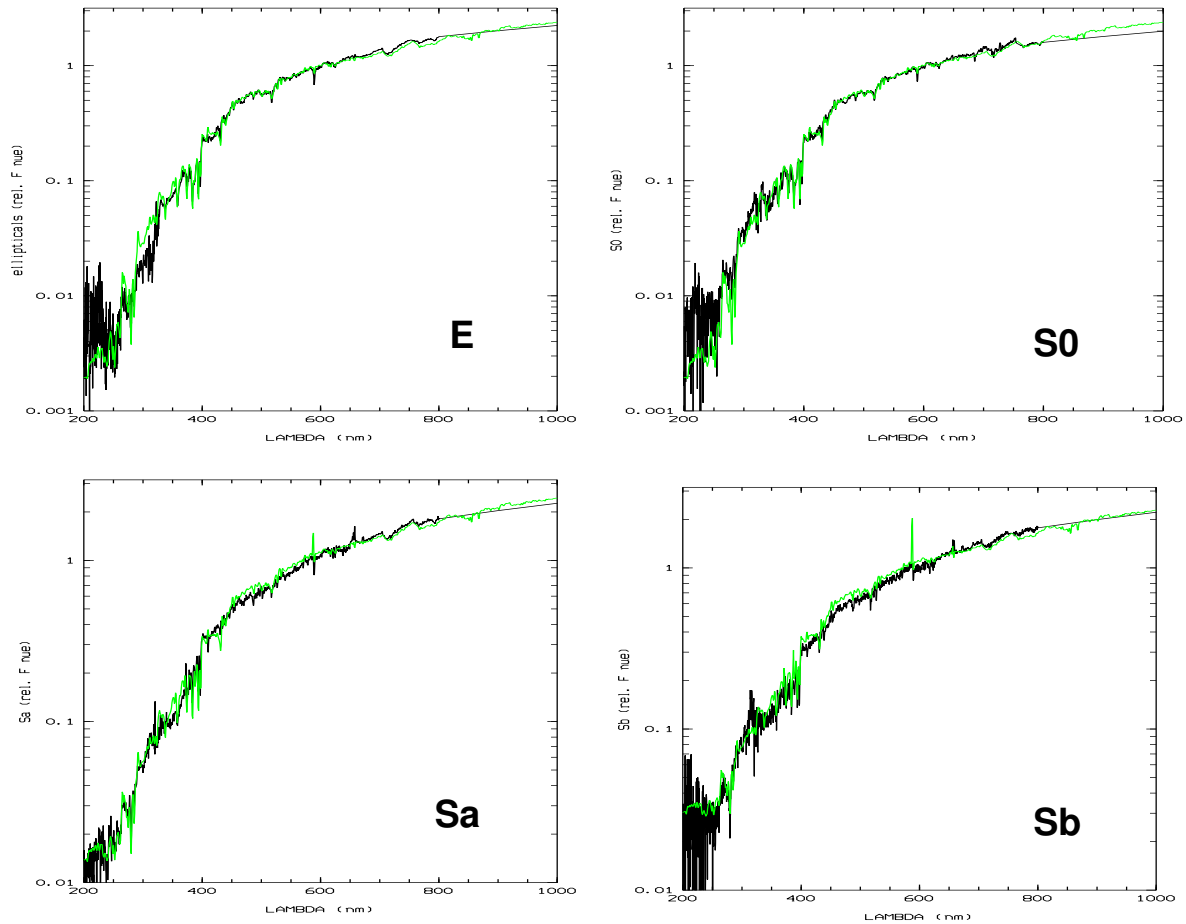
Figure 2.6: The galaxy types (E-Sb). The black curves represent the Kinney et al. spectra [Kinney et al. 1996]. The green curves are the best fits of the PEGASE spectra to the Kinney et al spectra. The fluxes are measured in F_ν, where the absolute flux calibration is chosen arbitrary. Since for the classification only the colors are needed, the flux calibration is not necessary.
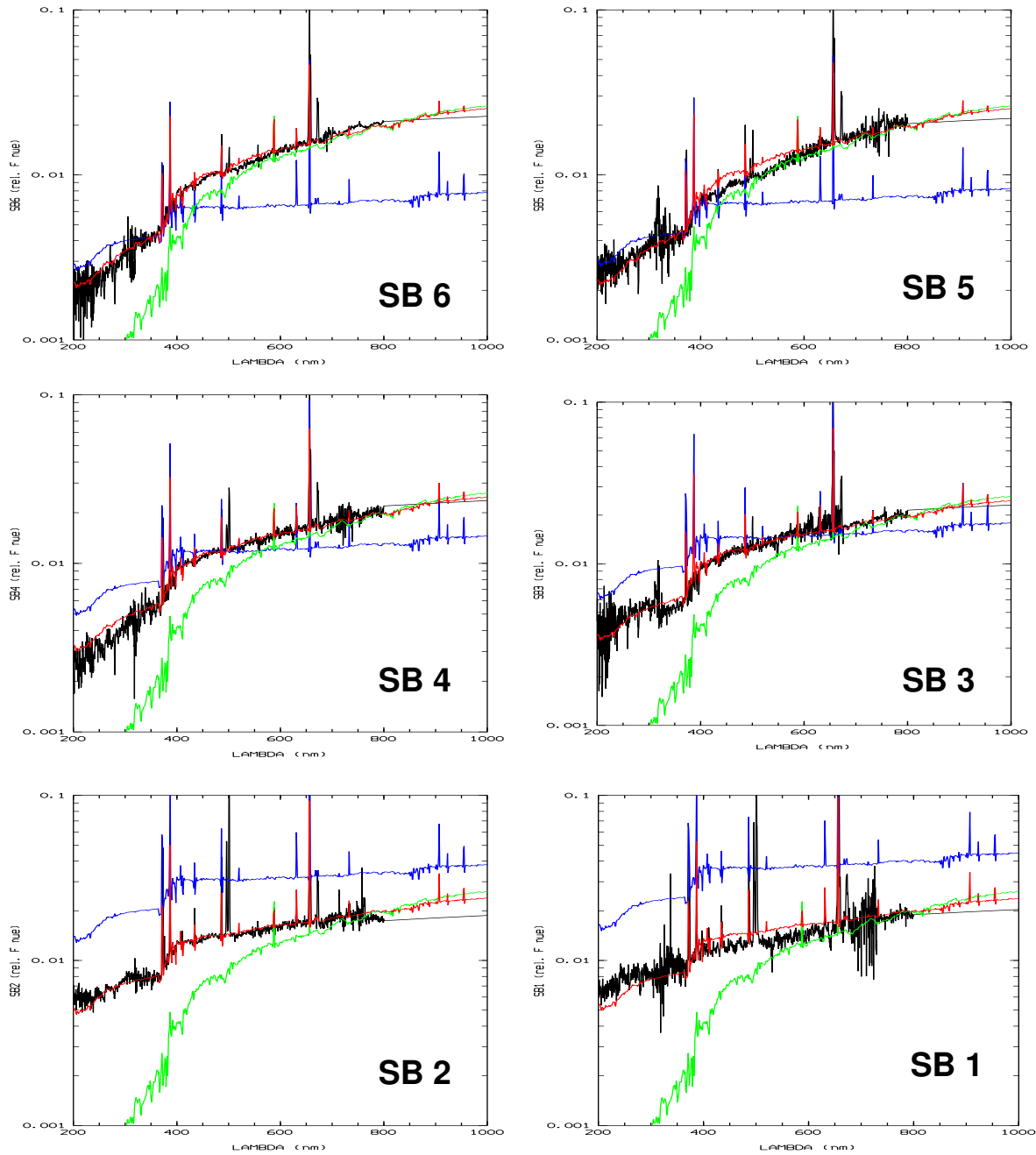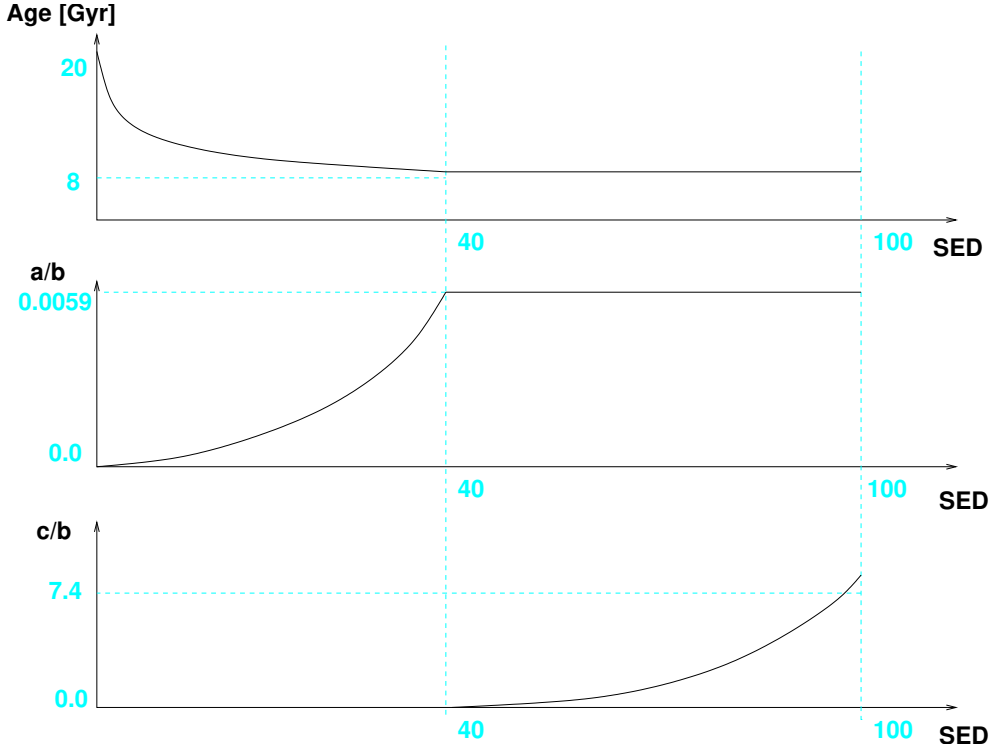
Figure 2.7: The starburst galaxies. The black curves represent the Kinney et al. spectra [Kinney et al. 1996]. The green curves are the old stellar population (it is always the Sb spectrum shown in figure 2.6). The blue curves are the starburst components. The red curves show the sum of the blue and green curves and are the best fits to the Kinney et al. spectra. The fluxes are measured in F_ν, where the absolute flux calibration is chosen arbitrary. Since for the classification only the colors are needed, the flux calibration is not necessary.

Figure 2.8: A scheme how the new library is constructed. SED 40 is the borderline between the galaxy types (E-Sb) and the starburst galaxies. The parameters are shown in figure 2.2. For the (E-Sb) galaxies the age decreases logarithmically, and the a/b ratio increases exponentially. These parameters are changed along the yellow line in the figure 2.3 and 2.4. For the starburst regime the c/b ratio increases exponentially (yellow line in figure 2.5).

2.5 The galaxy template library for classification

Based on the parameters derived in the last section I created a template library that is tailored for the purpose of multi-color classification. For this the library has to be continuous in color space. This means, that at a given redshift most of the colors have to be a monotonic function with the SED parameter in order to avoid wrong redshift estimations. If the color distribution is a non-monotonic function there may exist regions in the (SED,z) plane where the template colors fit to the object colors by accident better than at the right redshift. This may cause a redshift scattering towards entirely different values.

A second demand on the new library is that the astrophysical parameters should be a continuous and monotonic function of the SED parameter, because in this case it is possible to transform the error bars of the SED type into error bars of the considered parameter. These parameters are input parameters for the PEGASE-code. In the last section I presented the parameters derived from fitting the PEGASE spectra to the Kinney et al. spectra. The high suitability for multi-color classification of the Kinney et al. spectra has been already shown, so when this parameter set is used to create a new library one would expect similarly good results for the quality of redshift and SED information.

The library itself is constructed as shown in figure 2.8. The limit separating the (E-Sb) type galaxies and the starburst galaxies is chosen to be SED 40. The reason for that choice is to link them as close as possible to the Kinney et al. library given in [Wolf et al. 2001b]. Between SED 1 and SED 39 the age of the galaxies decreases logarithmically from 20 Gyr at SED 1 to 8 Gyr at SED 39. Over this SED range the law

$$\frac{age}{Gyr} = \frac{7.0 - \ln(0.019 \cdot SED)}{0.31} \tag{2.7}$$

is applied. The a/b ratio increases from zero at SED 1 to 0.16 at SED 39, and follows the law

$$\frac{a}{b} = \exp\left(\frac{SED}{13.3} - 4.7089\right) - 0.009 \tag{2.8}$$

In terms of star formation rate this corresponds to an a/b ratio of 0.0059 at SED 39. The SED types are distributed along the yellow lines as shown in the figures 2.3 for the ages and 2.4 for the a/b ratios. In these figures examples of the SED types are shown as yellow numbers. SED 1 corresponds to an elliptical and lenticular galaxy, whereas SED 39 is an Sb galaxy. The Sa galaxy is located at about SED 25. In the starburst regime the c parameter increases exponentially from zero at SED 40 to 0.5 at SED 95, whereas the d parameter is fixed to 60 Myr. From SED 40 on the law

$$c = \frac{\exp\left(SED \cdot 0.058\right)}{493} - 0.021 \tag{2.9}$$

is applied. Transformed to the SFR this corresponds to a maximum c/b ratio of 7.4. This is lower than the c/b range in figure 2.5, because this choice is better tailored to the COMBO-17 dataset in the sense that the SED range represents the measured colors. Again, the yellow line and the yellow numbers in figure 2.5 show how the SED types are distributed along the c parameter axis.

The spectra of the new template library are shown in figure 2.9. These spectra changes monotonously in almost any color between 200nm and 700 nm.

2.6 Comparison of the libraries

The new library described in the last section has to be proven to be as suitable for classification in COMBO-17 as the formerly used galaxy template library based on the Kinney et al. spectra. If this was the case one would be able to replace the Kinney et al. library by this new PEGASE library in the COMBO-17 multi-color classification process. The SED parameter determined in this way would contain the astrophysical information I described in the last section. Despite these parameters are ambiguous due to degeneracies, "robust" estimates such as the stellar M/L ratio [Bell & de Jong 2001] are possible.

First of all, a Monte Carlo simulation to check the redshift estimation for different magnitudes is carried out. The comparison of the redshift and SED classifications with both libraries should show differences and similarities.

The result of the Monte Carlo simulation is shown in figure 2.10 for three different R-band magnitudes. This means that a certain R-band magnitude is assumed and the magnitudes in the other filters are calculated by using the color library. This is done by taking the color library
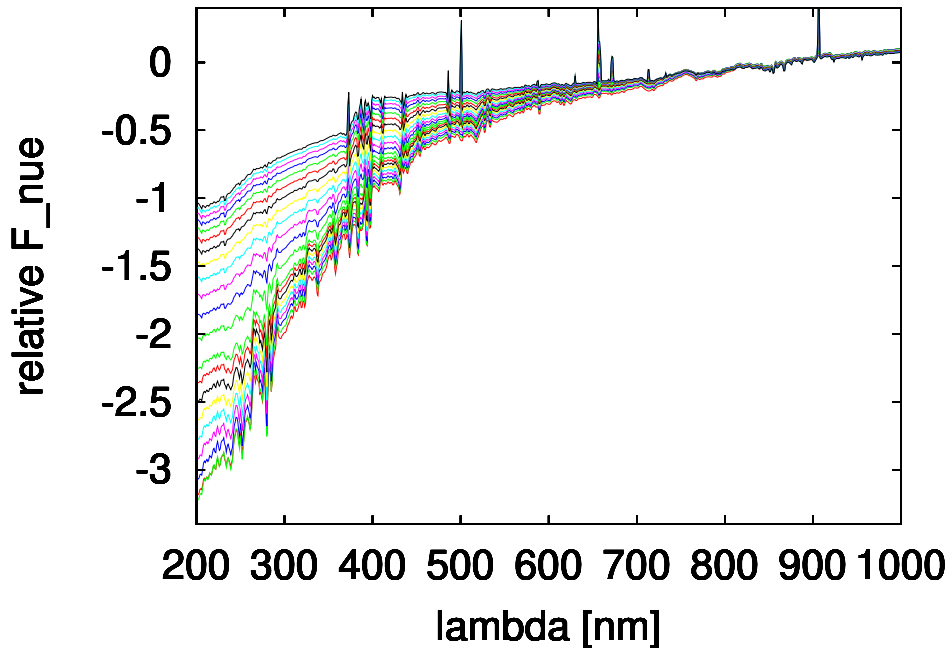
Figure 2.9: The galaxy template library based on the PEGASE spectra. In order to avoid overcrowding, instead of all SED types only the SED's 1,5,10,15,... are shown.

of the Kinney spectra and adding random errors to each color corresponding to the chosen magnitude. In a second step the so created "flux table" is classified by using the PEGASE library. It shows that for all magnitudes the redshifts are almost good reproduced with a certain scatter. There are also some artefacts, where some objects are scattered to higher redshifts.

Figure 2.11 shows the comparison of the redshift estimations for the real data in COMBO-17 in the classifications with both libraries. It seems that both libraries deliver within some scatter almost similar redshifts.

However, still a problem at redshifts above 1.0 remains, and it appears another problem at redshifts between 0.3 and 0.4. The comparison of the SED estimations is shown in figure 2.12. Above SED 40 both classifications behave similar, but below this borderline there is some scatter, and below SED 20 the Kinney SED's don't seem to match the observed SED's anymore.

The Abell 901 galaxy cluster, which is observed in one of the COMBO-17 fields, can be used for a first test of the quality of the redshift estimation. The cluster is located at redshift of about 0.16 so that a peak in a redshift histogram should appear there. This is shown in Figure 2.14. It shows a slight shift of the peak of about $\Delta z \sim 0.1$ in the sense that the classification with the PEGASE spectra delivers lower redshifts than the classification with the Kinney library. Furthermore the redshift distribution appears broader for the PEGASE classification.

Starting from the PEGASE library two different libraries were developed in order to improve the redshifts. These are:
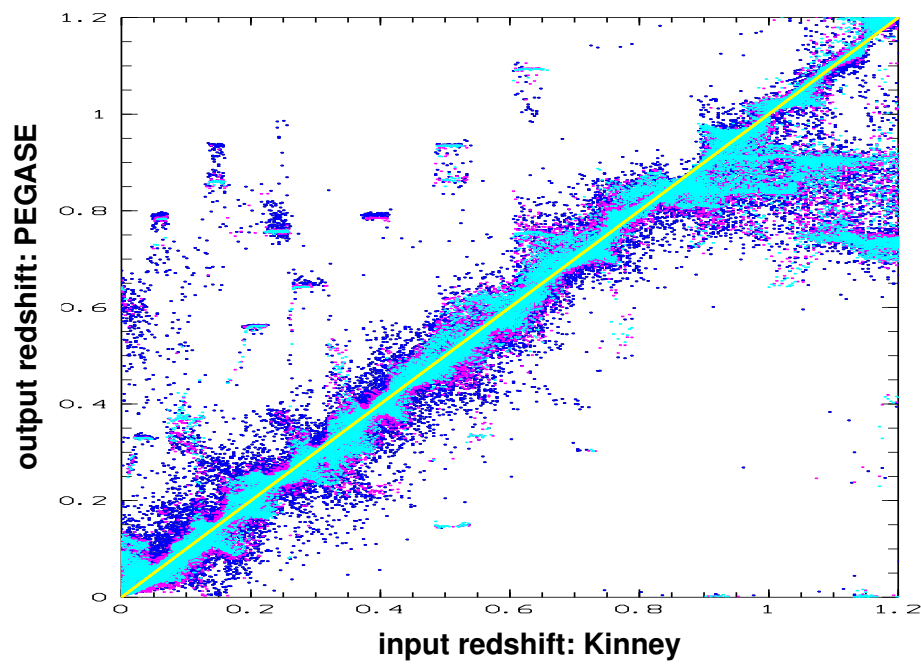
Figure 2.10: Monte Carlo simulation of the classification with the new library. The Kinney et al. spectra with given redshifts (x-axis) are Monte Carlo simulated and reclassified with the PEGASE library. The result of the redshift estimation is shown at the y axis. The colors show different R-band magnitudes: R = 23 in blue, R = 22 in purple and R = 21 in light blue.
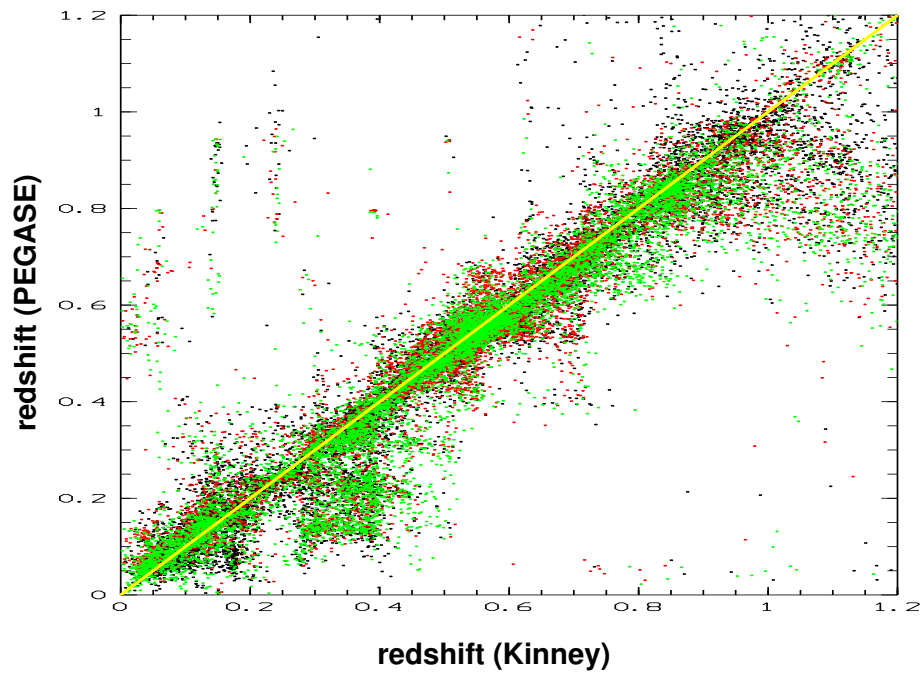
Figure 2.11: Comparison of the redshift estimation in both libraries. The x-axis are the redshifts in the classification with the Kinney library and the y-axis are the redshifts in the classification with the PEGASE library. The colors are the different fields: A901 in black, CDFS in red and S11 in green.
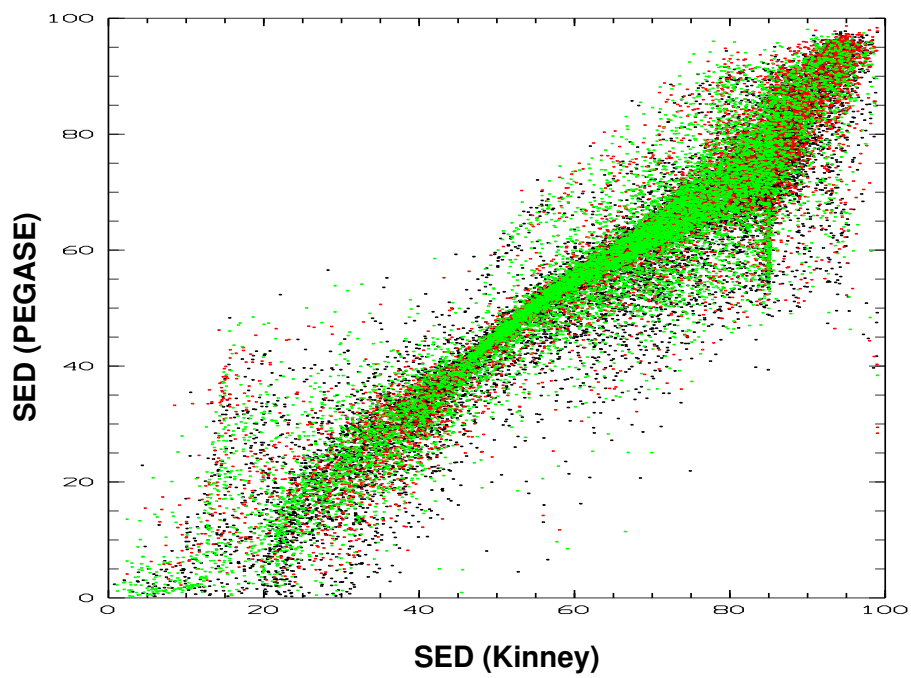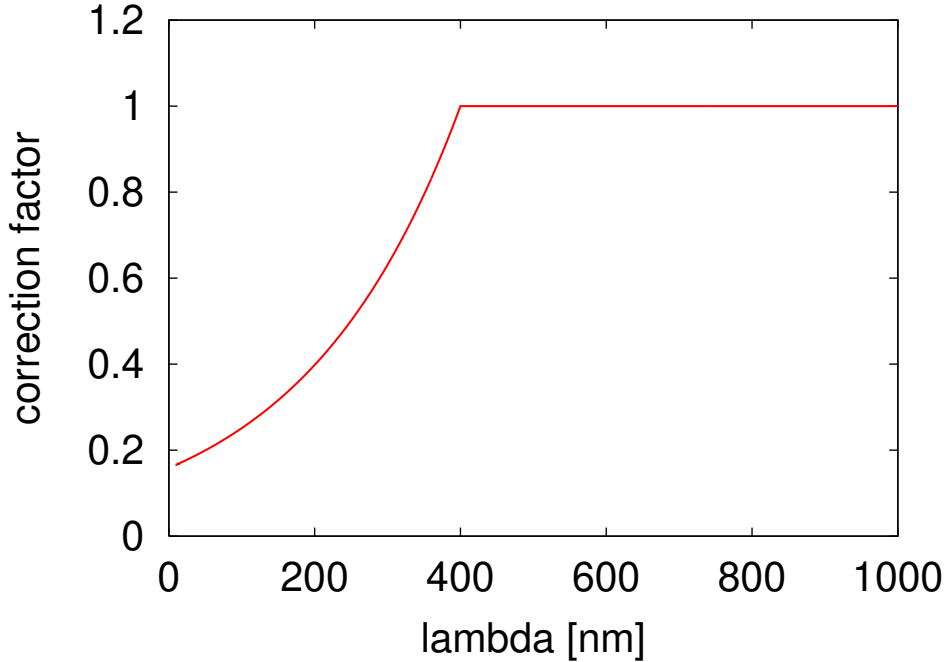
Figure 2.12: Comparison of the SED estimation in both libraries. The x-axis are the SED's in the classification with the Kinney library and the y-axis are the SED's in the classification with the PEGASE library. The colors represent the different fields: A901 in black, CDFS in red and S11 in green.

Figure 2.13: Conversion factor for converting the PEGASE library as described in section 2.9 into the F2003 library. Below 400 nm the factor corresponds to a magnitude difference of $\Delta m = 0.005 \cdot (400 - \lambda/nm)$ and above 400 nm the factor is 1.0.

- The F2003 library, which is tailored for the purpose of stellar mass estimation.

- The J2003 library, which is tailored for the purpose of redshift estimation.

The F2003 library differs from the PEGASE library described in section 2.5 by the magnitude difference $\Delta m = 0.005 \cdot (400 - \lambda/nm)$ at wavelengths below 400 nm. The corresponding conversion factor is shown in figure 2.13. This ad hoc correction is mainly empirically motivated. A comparison of the colors of the galaxies in the Abell 901 cluster with redhifts around 0.17 to those of higher redshifts (such as $z = 0.7$) shows that the colors of the PEGASE library do not fit to the measured colors both in the optical regime and in the UV regime at the same time. Therefore the correction of these spectra in the UV regime is necessary, as described above. One possible reason for this mismatch to the measured colors is that already the Kinney et al. spectra might have problems in the UV regime. Since the Kinney et al. spectra are IUE spectra glued to optical spectra there may be mismatches of the absolute flux calibration. The correction below 400 nm aims at matching the templates better to the observed COMBO-17 colors.

Figure 2.14 also shows the redshift distribution of the F2003 library. As shown in this figure it improves the redshift estimation dramatically in the sense that more objects are concentrated at values around the cluster redshift.

In figure 2.15 the SED classification with both libraries is shown for the respective redshifts around the A901 cluster. The PEGASE library classifies more elliptical and S0 galaxies (SED
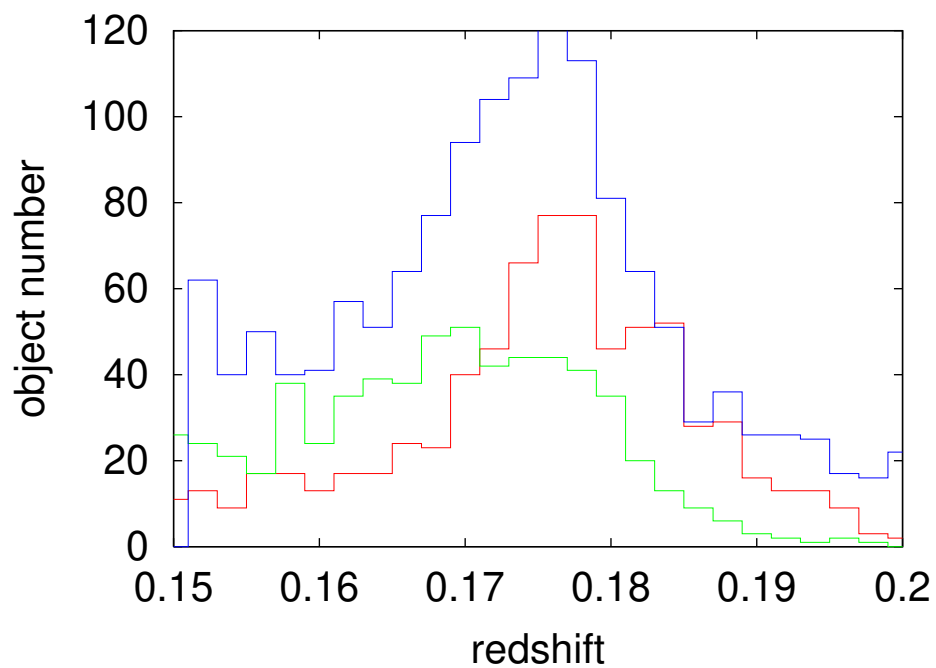
Figure 2.14: Histogram of the redshift distributions around the Abell 901 cluster. The red histogram shows the redshifts classified with the Kinney library and the green histogram shows the redshifts classified with the PEGASE library. The blue histogram is the redshift classification with the F2003 library.
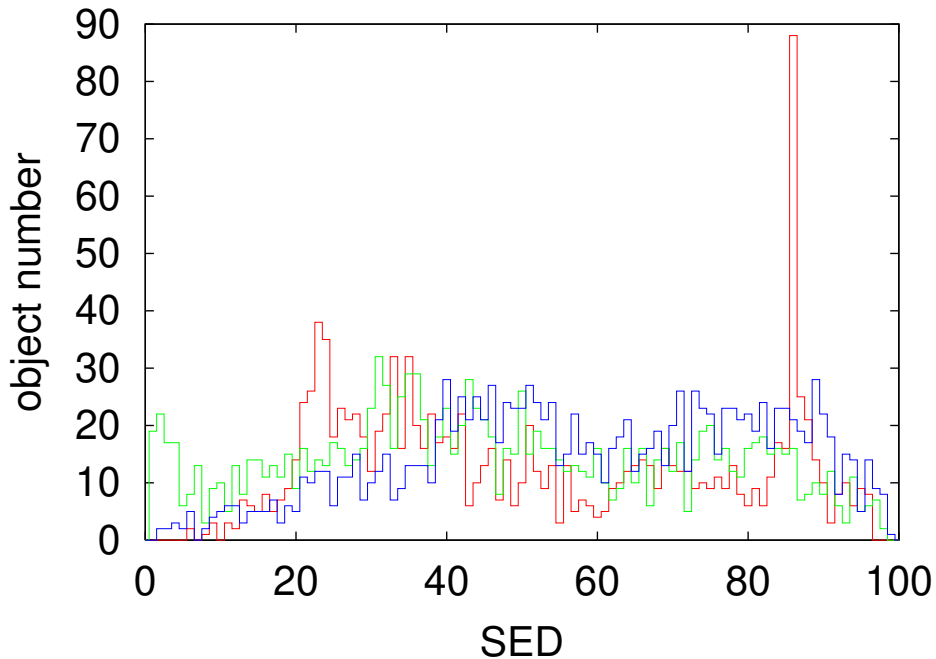
Figure 2.15: Histogram of the SED distributions around the Abell 901 cluster. The respective redshifts are selected to be in the range $0.15 \leq z \leq 0.2$. The red histogram shows the SED type classified with the Kinney library and the green histogram shows the SED classified with the PEGASE library. The blue histogram is the SED classification with the F2003 library.

below 20) than the Kinney library. Clusters contain in particular these types of galaxies and it seems, that the Kinney classification delivers a too low a number of them. However, the F2003 library delivers less galaxies than the PEGASE library at SED's below 20.

Figure 2.16 shows a comparison of spectroscopic and photometric redshifts for a classification with all three libraries. In the Abell 901 cluster the PEGASE redshifts are better, and in the S11 cluster they are worse. The PEGASE library produces a larger scatter towards lower redshifts. For example, in the Abell 901 cluster the PEGASE classification show some more outliers, whereas the F2003 library shows less outliers.
For Seyfert galaxies, as shown in figure 2.17, there is even a stronger trend to scatter towards lower redshifts. The F2003 library seems to heal this effect. For those objects of course both libraries deliver bad redshifts, because these kind of objects is not taken into account in the library which contains only galaxies without AGN's. Therefore for such objects a reliable redshift estimation cannot be expected.

In order to improve the photometric redshifts Christian Wolf developed another library that is called J2003 [Wolf et al. 2004]. This library is entirely different from the library described in section 2. It relies no longer on the original Kinney et al. library but is designed empirically in order to match the colors of measured COMBO-17 galaxies. Whereas the F2003 library is a one-dimensional sequence of spectra, the J2003 library is two dimensional: In one dimension it
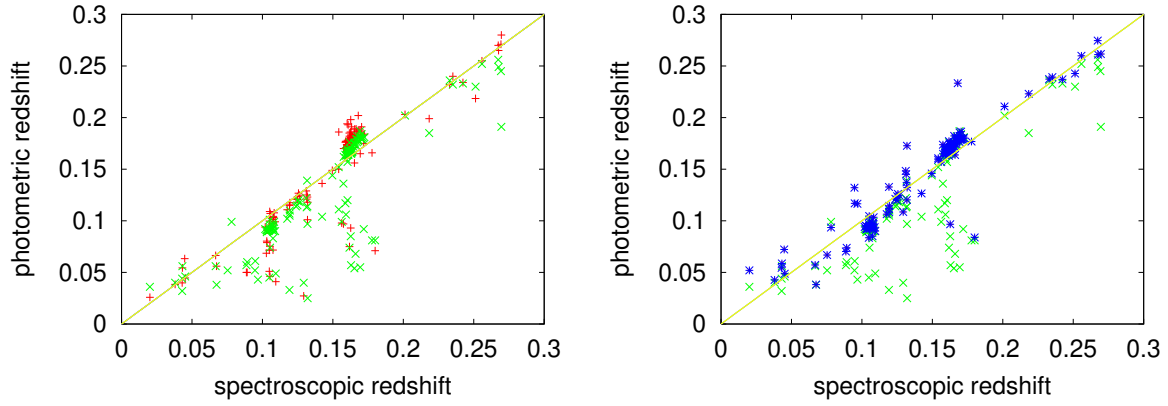
Figure 2.16: Comparison of photometric and spectroscopic redshifts for different classifications. In red the photometric redshifts for the classification with the Kinney et al. library is shown, whereas the photometric redshifts for the classification with the PEGASE library are shown in green. The F2003 classification is shown in blue in the right plot.
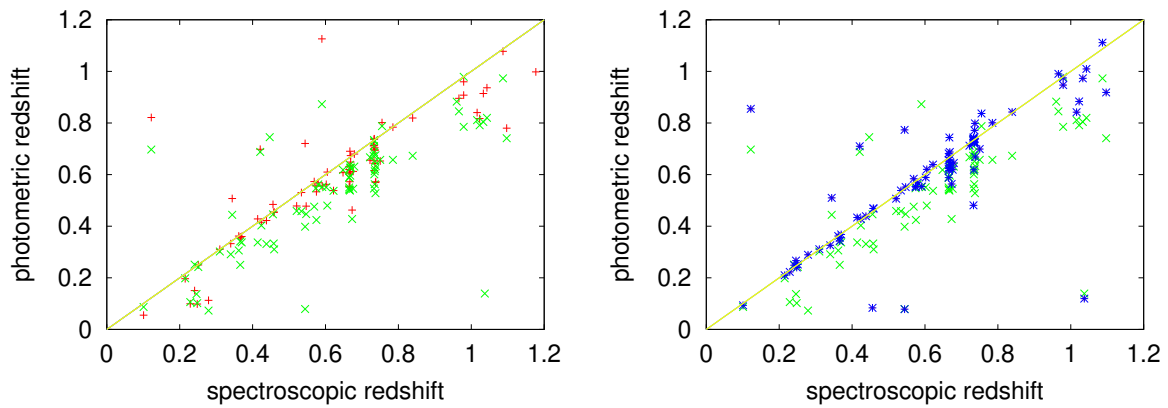

Figure 2.17: Comparison of photometric and spectroscopic redshifts for different classifications for Seyfert galaxies in the CDFS field. Objects which are classified as "Galaxies" with R-band magnitudes below 24.0 are taken into account. In red the photometric redshifts for the classification with the Kinney et al. library is shown, whereas the photometric redshifts for the classification with the PEGASE library are shown in green. The F2003 classification is shown in blue in the right plot.
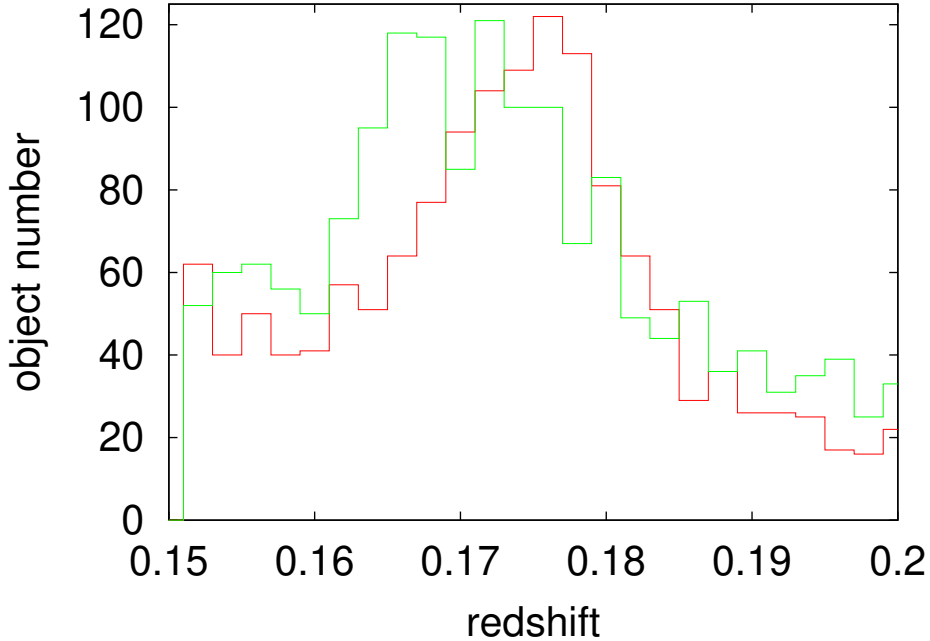
Figure 2.18: Histogram of the redshift distributions around the Abell 901 cluster with the F2003 library (red) and the J2003 library (green).

represents a sequence of different ages in the regime 50 Myr to 15 Gyr, and the other dimension takes a variation of the dust extinction into account by applying a law derived for the Small Magellanic Cloud. Figure 2.18 compares the F2003 and J2003 redshifts in the A901 cluster, which is the same test as in figure 2.14. Figure 2.19 shows the comparison of the J2003 and the F2003 libraries to the spectroscopic redshifts. As one can see, the J2003 library delivers a better redshift estimation.

In summary, the F2003 library is a considerable improvement compared to the Kinney et al. library that was originally used for classification in COMBO-17. The F2003 library delivers better redshifts than the PEGASE library, but worse redshifts than the J2003 library. Hence, the J2003 library yields the best redshifts and is therefore used for the redshift estimation by the COMBO-17 team and the GEMS team.

Unfortunately, the J2003 library is not suited for stellar mass estimation, because it is purely driven by matching colors by any kind of spectra but not by using an astrophysical reasonable assumption about star formation histories. For the purpose of stellar mass estimation a good assumption for the underlying old stellar population of starburst galaxies is needed. The colors of these galaxies may be dominated by hot stars of the young stellar population, but an old stellar population usually dominates the stellar masses. The F2003 library does assume an old stellar population for starburst galaxies. This assumption may be a better approach than a single young stellar population that is assumed for the J2003 library. For this reason I use the F2003 library for the stellar mass estimation as described in the next Chapter. This method
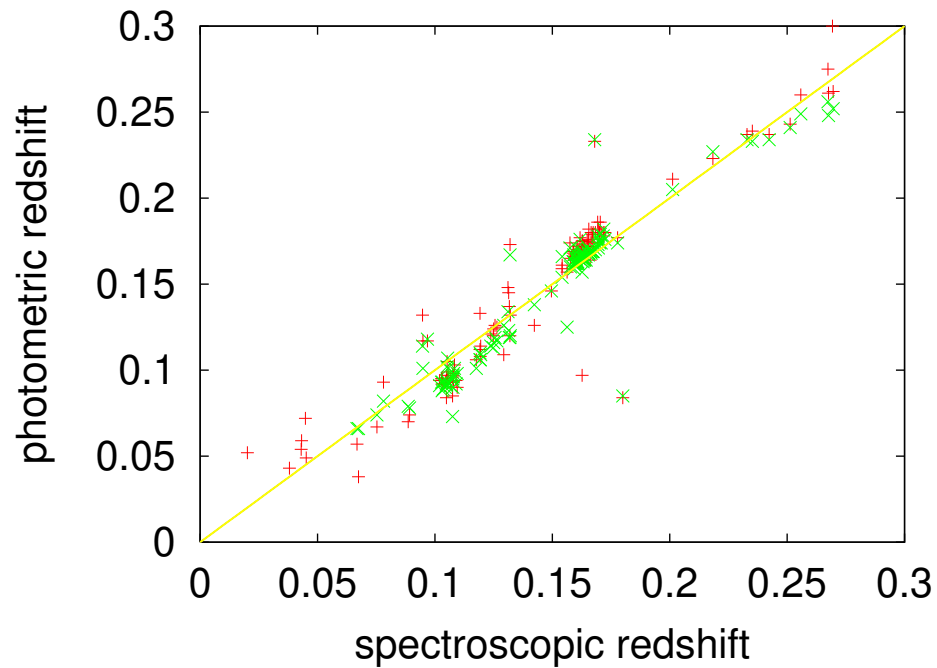
Figure 2.19: Comparison of photometric and spectroscopic redshifts for classifications with F2003 (red) and J2003 (green).

is self consistent in the sense that the F2003 library is applied for the multi-color classification. In order to link this method to the J2003 redshifts which became standard in COMBO-17, I developed the "piggyback" method, which is described in chapter 4.

Chapter 3

The stellar masses of galaxies

In this chapter the method of stellar mass estimation is described. In principle, the fluxes of one COMBO-17 filter are transformed to stellar masses by using a stellar M/L ratio, which is determined by the SED parameter. For this purpose the F2003 library described in the last chapter is used both for the multi-color classification and for the estimation of the stellar masses as described here. In section 3.1 a formula is derived that calculates the stellar masses from the three components of the star formation rate (Figure 2.2). Section 3.2 will test the robustness of the stellar masses estimated in this way. In section 3.3 the results are presented.

3.1 Estimation of the stellar mass

3.1.1 The method of stellar mass estimation

The method of measuring the stellar mass is based on the fact that reliable redshift and SED estimations are available for the COMBO-17 galaxy sample. The expected accuracy of the redshift estimation is shown in Wolf et al. [Wolf et al. 2001b]. The SED errors and their dependence on the redshift errors is discussed in the next section.

The flux measurement in the COMBO-17 filter with the longest central wavelength is used (see figure 2.1). Since in the 915 nm filter the S/N ratio is low, the filter with a central wavelength of 816 nm and a width of 24 nm is chosen. As a comparison, the 5σ-limits of the Vega magnitudes in the 915 nm filter range from 22.6 to 23.0 in three different COMBO-17 fields, whereas the 816 nm filter has a limiting magnitude of 23.6 in all fields. The central wavelength defines the maximum redshift where the stellar mass can be measured reliably. The stellar mass has to be estimated at every redshift from a flux point at a restframe wavelengths longer than the 4000Å break. Therefore the investigation of this work is limited to redshifts below 1.0.

The flux, which is given in the unit $\gamma m^{-2} s^{-1} nm^{-1}$ [Wolf, PhD thesis] is derived from the photometry package MPIAPHOT. It measures the flux in a fixed aperture by convolving the flux to an effective PSF of 1.5 arcseconds. In the R-band filter in addition the SExtractor MAG-BEST magnitudes are available. They are used to calculate correction factors ΔF_{tot} which correct the fixed aperture measurement to an isophotal shape. Applying the ΔF_{tot} factor is strictly speaking only in the R-band a good correction, but it is also applied to the 816 nm filter in order to correct approximately for aperture effects.

The main idea of the stellar mass estimation is to compare the measured flux in the 816 nm filter with the flux predicted by the PEGASE code in this filter at the redshift of consideration. In the following the formula which calculates the stellar mass from the 816-flux F_{phot}, the redshift

z and the luminosity distance D_L as input parameters is derived. It takes the SED parameter in the form of its translation to the parameters a, b and c as presented in section 2.4 into account. First, the theoretically expected apparent flux $F_{\lambda,object}$ is calculated from the flux delivered from the PEGASE code, which is normalized in such a way that the stellar population has a mass of 1 $M_\odot$. In the following equation the sum of the sum of the three components in figure 2.2 is considered as F_λ, its assembly will be described below.

$$\frac{\int F_\lambda \cdot S_\lambda \, d\lambda \cdot \frac{1}{m}\frac{M}{M_\odot}}{\int S_\lambda \, d\lambda} \cdot \frac{1}{4\pi D_L^2 (1+z)} = F_{\lambda,object} \tag{3.1}$$

The integral limits in this formula are 0 to ∞. The filter function S_λ gives the transmission of the 816 filter, which is a non-vanishing function in the regime around 816 nm, because the filter has a fixed central wavelength. The flux of the object may be redshifted and hence the wavelength scale of the flux $F_{\lambda,spectrum}$ is shifted by the factor $(1+z)$. The normalization factor m will be declared later. The flux F_λ is given here in the unit $erg\,m^{-2}\,s^{-1}\,\text{Å}^{-1}$ and can be transformed with the formula:

$$F_{phot} \cdot \Delta F_{tot} = \frac{\lambda}{hc} F_\lambda \tag{3.2}$$

With (3.2) formula (3.1) transforms to

$$\frac{\int F_\lambda \cdot S_\lambda \, d\lambda \cdot \frac{1}{m}\frac{M}{M_\odot}}{\int S_\lambda \, d\lambda} \cdot \frac{1}{4\pi D_L^2 (1+z)} = \frac{hc}{\lambda} F_{phot} \Delta F_{tot} \tag{3.3}$$

Solving this formula for the mass leads to:

$$\frac{1}{m}\frac{M}{M_\odot} = \frac{F_{phot}\,(1+z)\,\Delta F_{tot} \cdot 4\pi D_L^2 \cdot \frac{hc}{\lambda} \int S_{\lambda,spectrum}\, d\lambda}{\int F_{\lambda,spectrum} \cdot S_{\lambda,spectrum}\, d\lambda} \tag{3.4}$$

In order to normalize the mass, the total stellar mass in the simulated stellar population has to be calculated. Therefore the model for the star formation history as shown in figure 2.9 is taken into account. The total stellar mass results from a linear combination of the individual components with the parameters a, b and c.

$$m = a \cdot A + b \cdot B + c \cdot C \tag{3.5}$$

Here A, B and C are the stellar masses of the respective components. A similar linear combination has to be made for the spectral fluxes as well. The integral in (3.4) is calculated in the following way:

$$\int F_\lambda \cdot S_\lambda \, d\lambda = a \cdot \int F_{\lambda,a} \cdot S_\lambda \, d\lambda$$
$$+ \quad b \cdot \int F_{\lambda,b} \cdot S_\lambda \, d\lambda + c \cdot \int F_{\lambda,c} \cdot S_\lambda \, d\lambda \tag{3.6}$$

When (3.5) and (3.6) are inserted in equation (3.4), the final result will be:

$$\frac{M}{M_\odot} = \frac{F_{phot}\,(1+z)\,\Delta F_{tot} \cdot 4\pi D_L^2 h_{70}^{-2} \cdot \frac{hc}{\lambda}}{\frac{a}{A} \cdot \frac{\int F_{\lambda,a}\cdot S_\lambda\, d\lambda}{\int S_\lambda\, d\lambda} + \frac{b}{B} \frac{\int F_{\lambda,b}\cdot S_\lambda\, d\lambda}{\int S_\lambda\, d\lambda} + \frac{c}{C} \frac{\int F_{\lambda,c}\cdot S_\lambda\, d\lambda}{\int S_\lambda\, d\lambda}} \tag{3.7}$$

The Hubble constant is chosen as $H_0 = 70 \cdot h_{70} \, km/(s \, Mpc)$ following the convention of Rich, where $h_{70} = 1$ for a $H_0 = 70 km/(sMpc)$ universe. Since the fluxes of the PEGASE spectra are normalized to 1 $M_\odot$, they are divided by the stellar masses A, B and C in each component. Hence, equation (3.7) delivers the stellar mass estimates for a given flux, a given redshift and a given SED = SED(a,b,c).

3.1.2 Error analysis

The errors of the stellar masses depend on the errors of the redshift σ_z and of the SED parameter σ_{SED}. These two parameters are not independent of each other. Figure 3.1 shows an example of the mutual dependence of these parameters. In order to take into account the mutual dependence the covariance matrix is calculated for each of the measured galaxies. For this purpose the redshift is used, which is obtained from the multi-color classification. This particular redshift is assumed to be appropriate for the object of consideration. Next, the SED parameter is classified again, but in this case the redshift is fixed and the SED parameter is the only degree of freedom. This is done for the particular value where the redshift was estimated at the first time, and also for a certain region around it. The result for a certain object is shown in figure 3.1. the covariance matrix

$$C = \begin{pmatrix} P_i^2 \overline{(z_i - \overline{z_i})^2} & P_i^2 \overline{(sed_i - \overline{sed_i})(z_i - \overline{z_i})} \\ P_i^2 \overline{(z_i - \overline{z_i})(sed_i - \overline{sed_i})} & P_i^2 \overline{(sed_i - \overline{sed_i})^2} \end{pmatrix} \tag{3.8}$$

is calculated by using all the points (z_i, sed_i) shown in figure 3.1. These points are weighted by the probabilities

$$P_i = exp \left[-\frac{1}{2} \left(\frac{z_i - z_{orig}}{\sigma_z} \right)^2 \right] \tag{3.9}$$

where z_{orig} is the redshift of the original classification and σ_z is the redshift error. This matrix has to be diagonalized to obtain independent new parameters P and Q. The error estimation is done by using a gaussian error propagation in these new parameters:

$$\sigma_M = \sqrt{\left(\frac{\partial M}{\partial P} \sigma_P \right)^2 + \left(\frac{\partial M}{\partial Q} \sigma_Q \right)^2 + \left(\frac{\partial M}{\partial F} \sigma_F \right)^2}, \tag{3.10}$$

where the last term is the flux error σ_F which is considered to be in good approximation independent of the errors σ_P and σ_Q.

3.2 Robustness of the mass estimation

To what extent one can trust the stellar mass estimation depends first of all on the robustness of the M/L ratio delivered by the stellar population synthesis code itself. In this context one has to be careful about the astrophysical parameters put into the code and their degeneracies. Different star formation histories with different M/L ratios may lead to the same multi-color or even spectral properties. But even when the star formation histories are well constrained, there remains the issue of how to trace stellar mass from light at different wavelengths.
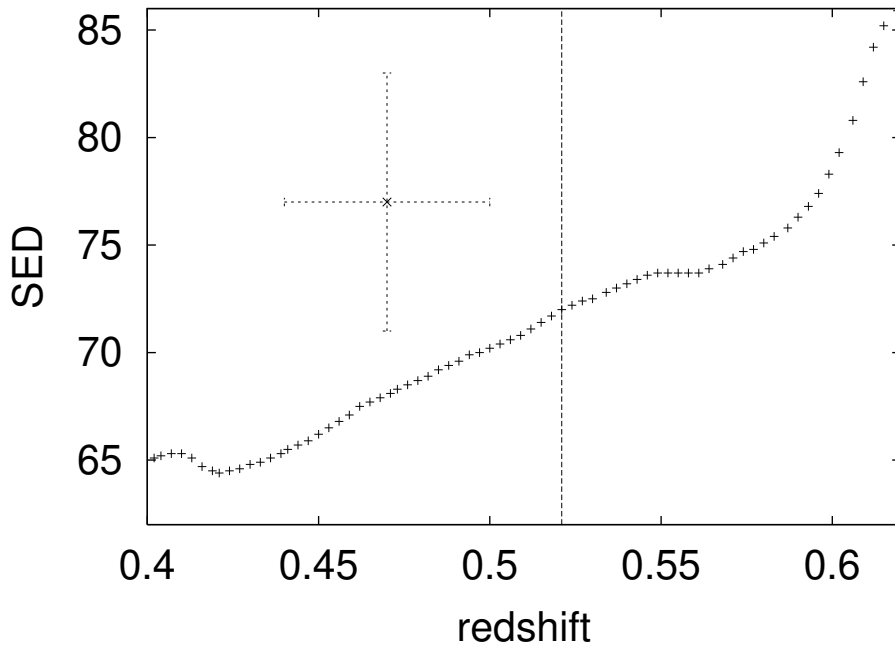
Figure 3.1: The mutual dependence of the parameters z and SED for a particular survey object: I firstly classify the object by using the COMBO-17 multi-color classification code. This leads to the redshift given at the dashed line. In a second step, I keep the redshift fixed at this particular redshift and apply again the multi-color classification routine. This time the SED type is the only degree of freedom. On the y-axis the reclassified SED parameter is plotted. I do it not alone for this particular redshift, but also for a certain regime around this redshift. The errorbar shows typical errors of the z and SED parameters for an object with $m_{816} = 22.5$.
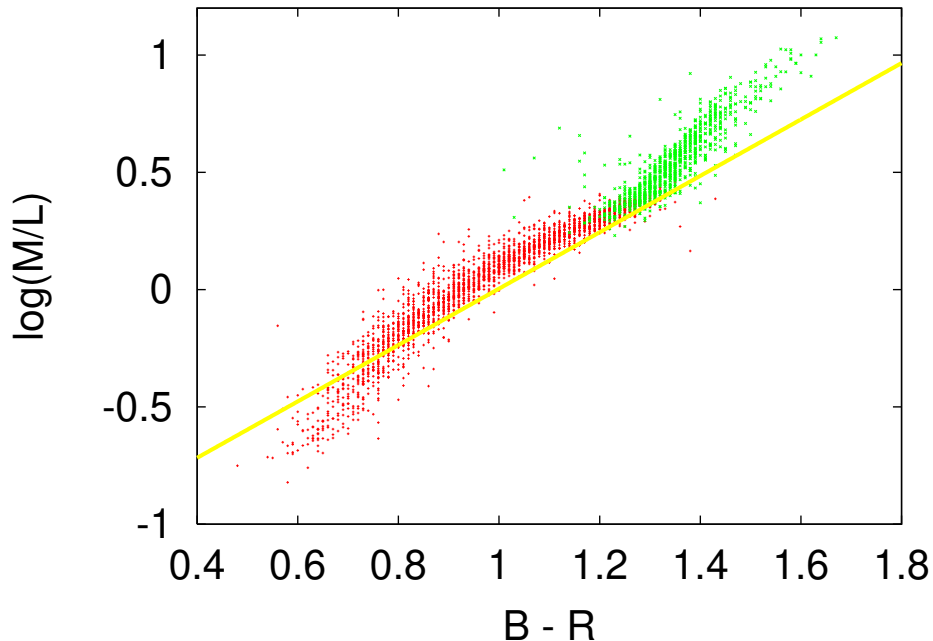
Figure 3.2: B-Band mass to light ratio vs. (B-R) color of *measured* COMBO-17 objects. As a comparison the line shows the Bell & de Jong [2001] result. The green points are SED types below 40 and the red points are SED types above 40.

3.2.1 Constraining the star formation histories

In figure 2.2 the assumed model of the star formation history (SFH) is shown. The multi-color classification constrains the galaxies to belong to a certain SED type, for which the parameters of the SFH are fixed. Nevertheless, it is not possible to break the parameter degeneracies occurring in stellar population models. In the case of the age-metallicity-dust degeneracy the increase of each of these parameters causes the galaxies to be redder. The effect can be compensated by decreasing another parameter. Despite the fact that the parameters describing a certain SED type simply represent one single point in parameter space, one should always be aware that due to these degeneracies the SED type actually represents certain regions in the parameter space that have the same properties in the 16 colors.

Bell & de Jong [2001] argue that the M/L ratio depends to the first order only on an optical color. The effect of dust extinction is both that it makes the galaxy fainter and it makes the galaxy redder. Whereas the first effect increases the mass-to-light ratio, the second effect causes a redder optical color and therefore a lower mass-to-light ratio produce the same optical color as in the case without extinction. When summing up these two effects the M/L ratio is little affected by dust extinction on the first order.
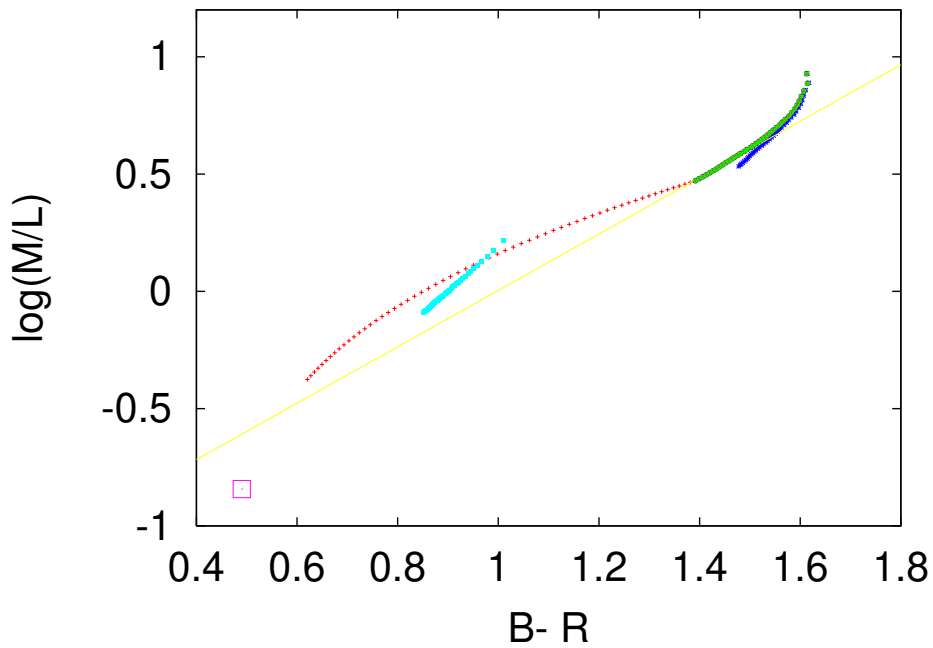
Figure 3.3: B-band mass to light ratio vs. (B-R) color *derived* with the `colors.f` code. The red dots show (E-Sb) type galaxies and the dark blue dots show starburst galaxies for *combined* stellar populations . The result for *single* stellar populations is shown as the green points for the initial burst component and in blue points for the constant star formation rate and the purple square shows the young stellar population. As a comparison the line shows the Bell & de Jong [2001] result.

3.2.2 The calibration of the stellar masses

In order to investigate the absolute calibration of the stellar mass estimations are compared both to the M/L ratios of Bell & de Jong [2001] and to the stellar mass fraction of the local universe of Kauffmann et al. [2003]. Bell & de Jong found a correlation between the M/L ratio and for example the (B-R) color. In figure 3.2 the B-band M/L ratio in dependence of the (B-R) color is plotted for all galaxies with stellar masses above $10^9 M_\odot$ and for redshifts below $z = 0.307$. This is the highest redshift with well defined restframe (B-R) color. The comparison to the Bell & de Jong result shows that most of the galaxies match within about 0.1 dex. The linear behavior proposed by Bell & de Jong [2001] is reproduced to first order, whereas higher order effects lead to deviations in particular at the red and blue end. This is mainly explained by the fact that in this work I deal with mixed stellar populations while Bell & de Jong investigated simple stellar populations. The assumption of mixed stellar populations is a more realistic approach at least for starburst galaxies. Note that the B-band M/L ratios are not simply derived by the PEGASE code, but compare two independent measurements, namely the stellar mass of the galaxies and the restframe B-band luminosity. In order to ensure that not only the absolute calibration but also the shape of the measured M/L vs (B-R) dependence is measured correctly, it is compared to a somewhat independent way of deriving the M/L ratio by using the `colors.f` code from the PEGASE package to derive the color and the B-band luminosity for each SED type. Figure 3.3 shows the thus obtained results for the M/L ratio in dependence of the color. The results of figure 3.2 and figure 3.3 show a good agreement, in particular the shape of the curve is similar to that of the measured data. Therefore the measured M/L ratio in the B-band reproduces the prediction of the PEGASE package.

Another test of the absolute mass calibration is the comparison of the fraction of the total stellar mass in galaxies estimated from the COMBO-17 data in the lowest redshift bin and from 10^5 SDSS galaxies by [Kauffmann et al. 2003]. To cover only field galaxies the cluster galaxies in the COMBO-17 field with the A901 cluster have to be taken out by cutting out the galaxies at redshifts between 0.15 and 0.2 in the A901 field. Figure 3.4 shows the resulting mass fractions in a histogram. The mismatch of the absolute calibration of the stellar mass estimations of this work and the [Kauffmann et al. 2003] results is of the order of 0.1 dex.

However, the two tests described above compare only mass estimations by using one stellar population synthesis model with mass estimations by using another stellar population synthesis model. Therefore they should rather be considered as self-tests in order to rule out obvious errors in our method. In order to get an independent test of the stellar mass estimation, the measured M/L ratio is compared to the value of our galaxy. In [Binney & Merrifield 1998] the value M/L $\approx 2.3\,M_\odot L_\odot^{-1}$ is given in the B-band, derived with a surface density of the ocal disk of $\Sigma_d = 48 \pm 9 M_\odot pc^{-2}$ [Kuijken & Gilmore 1991]. Since I am only interested in the stellar component, I use rather the value $\Sigma_\star = 24 \pm 3 M_\odot pc^{-2}$ for main sequence stars [Méra et al. 1998]. Hence, this leads to a value of M/L $\approx 1.15\,M_\odot L_\odot^{-1}$. One should keep in mind that this is only the disk value and neglects the bulge contribution. This value can be compared to the M/L estimation in this work. Since the Galaxy is a Sbc type [Binney & Merrifield 1998] and since the local value may be more representative for pure disks I expect the SED type to be classified between 50 and 70. Figure 3.5 shows the M/L estimation for nearby galaxies in this regime. The typical value is about M/L $\approx 1.0 \ldots 2.0\,M_\odot L_\odot^{-1}$. The expected value of M/L ≈ 1.15 lies close to the center of the considered SED interval.
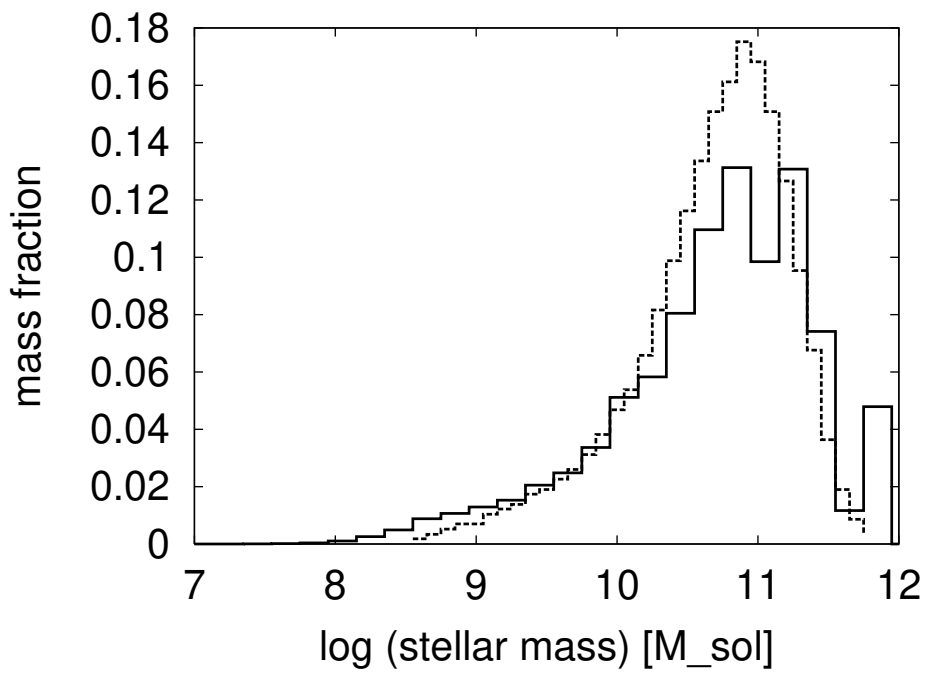
Figure 3.4: The fraction of total stellar mass in galaxies in the redshift regime $0.1 <$ $z < 0.3$ estimated with the COMBO-17 data (solid histogram).   As a comparison the [Kauffmann et al. 2003] result for SDSS galaxies is shown in the dashed histogram.
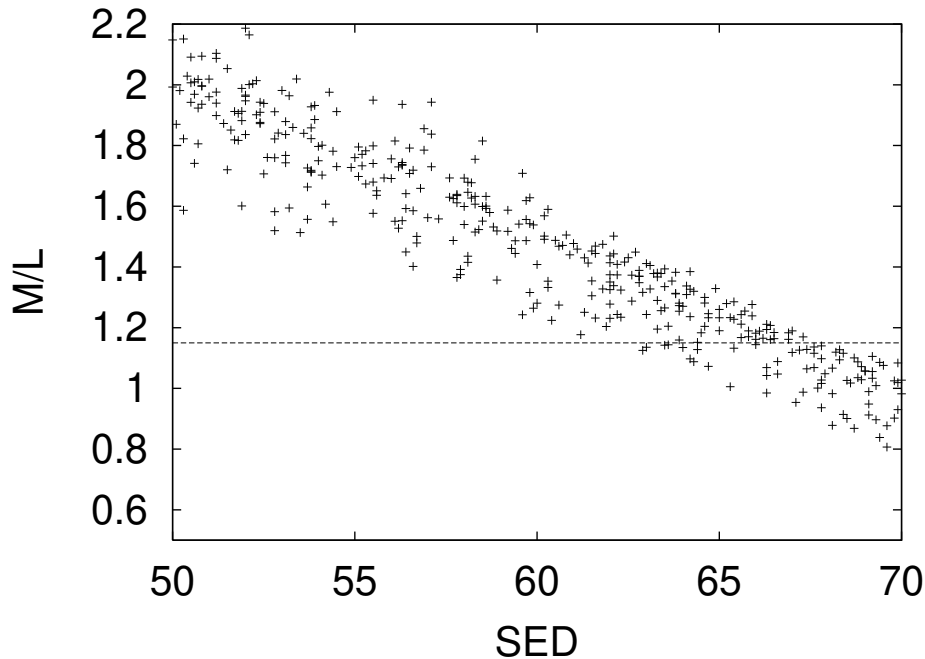
Figure 3.5: The B band M/L ratio versus SED for galaxies with redshifts of $0.1 < z < 0.2$ and SED types of $50 < SED < 70$. The dotted line shows the value I expect for the galaxy.

In summary, there is a mismatch of 0.1 dex between the stellar masses in this work and the predictions of Bell & de Jong, there is again a mismatch of 0.1 dex when comparing it to the Kauffmann et al. result, and also the result in figure 3.5 might be better when shifting by 0.1 dex. Thus, the stellar masses derived with the method of this work seems to be 0.1 dex or 25 % higher than the mass estimates from other methods.

3.3 Results

In this section the results of the stellar mass estimates are presented. I start with the results from the infrared data in order to test the quality of the mass estimations in the optical regime. For this purpose the stellar mass estimation in the infrared regime is compared to the estimation in the optical regime. This is possible for a subsample of about 400 galaxies. Thereafter I present the results of the mass estimations in the optical regime for the whole sample of galaxies.

3.3.1 Mass estimation from infrared data

As a part of the ESO Imaging Survey EIS [Hatziminaglou et al 2002] there are ISAAC data in the Chandra Deep Field South (CDFS) is publicly available. The limiting 5σ Vega magnitudes are J< 24.8, H< 23.4, and $K_s < 22.2$. So far, 8 pointings of ISAAC fields are reduced and publicly available, this leads to a field of view of 50 square arcminutes. Hence, only a small part of one COMBO field of view (32'×32') is available. Nevertheless, for a small subsample of

about 400 COMBO-17 galaxies I can compare the mass estimates directly derived from infrared photometry with those obtained in the optical regime.

Since the EIS data are already reduced and flux calibrated, these data are fed directly in the COMBO-17 pipeline and adjust the flux by using main sequence stars in this field. The field distortions of the ISAAC camera are corrected radially symmetric by using bright objects from a SExtractor table obtained from our R-band images of the CDFS.

In total the stellar masses of 400 galaxies in the eight ISAAC fields can be reliably estimated both in the 815 nm filter and also in the J, H and K_s ISAAC filters. The stellar mass estimation works as follows: The SED and redshift parameter is estimated by using the COMBO-17 multi-color classification with the 16 optical colors available in COMBO-17. The SED type delivers the stellar M/L ratio in the filters 815 nm, J, H and K_s. Together with the fluxes in these filters the stellar mass estimation is done in each of these filters. Hence, the SED and redshift estimations are the same for the stellar mass estimations in the optical and in the infrared. Both mass estimations differ only in the wavelength regime where the stellar M/L ratio is applied to the measured fluxes. This approach has the advantage, that it looks only for bandshifting effects when comparing both stellar mass estimations. The comparison between both mass estimations is shown in figure 3.6. It shows the difference between them as a function of SED type. The agreement is on average better than 0.1 dex for SED types below 70. For SED > 70 there is an offset of about 0.15 dex. The origin of the scatter for individual objects is partly due to the errors of the mass estimation. Figure 3.7 shows the difference divided by the mass error σ_M derived from section 3.1.2. The average difference hardly exceeds 1σ for the J and H band and increases to 2σ for the K band.

This leads to the conclusion that our PEGASE templates are a well-suited description to the entire observed wavelength range $0.8 < \lambda_{obs} < 2.1\mu$m.

3.3.2   Mass estimation from optical data

The results of the stellar mass estimation of the COMBO-17 galaxies with a limiting magnitude of 23.0 in the 815 nm filter (S/N > 8.7) as a function of redshift is shown in figure 3.8. The location of the Abell 901 cluster is clearly seen as a stripe at a redshift of about 0.17. The sharp cut-off at the lower mass end occur because of the magnitude limit of the survey. For redshifts around 0.2 stellar masses above $10^8 M_\odot$ are measurable whereas at redshift 1 only objects with stellar masses above $3 \times 10^9 M_\odot$ are included in the sample. The fuzzy boundary at the high mass end shows that at all redshifts objects exceeding $3 \times 10^{11} M_\odot$ are rare.

The error distribution of these objects as derived in section 3.1.2 is shown in figure 3.9. 71% of the galaxies have relative errors below $\sigma_M/M = 0.5$. The median error is about $\sigma_M/M = 0.29$. Figure 3.9 shows the error distribution at different mass cuts. It shows the trend that the higher the stellar masses of the objects (i.e. their luminosities) the lower are the relative errors.

I use the estimated stellar masses at redshifts up to $z = 1.0$ to derive the evolution of the stellar mass function. For this purpose the number counts are divided by the comoving volume, which is given by
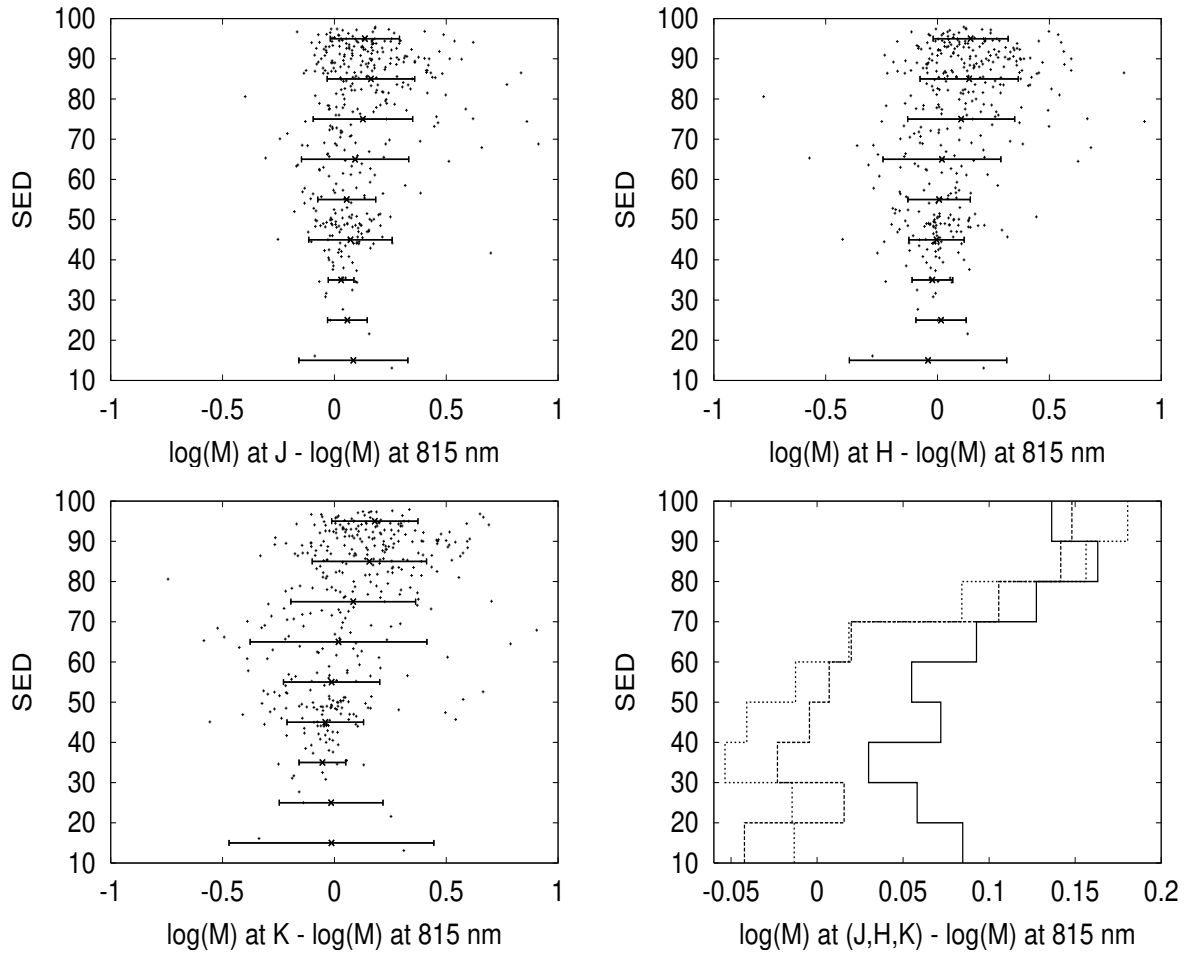
Figure 3.6: Difference between the stellar mass estimation in the infrared and the stellar mass estimation at the 815 nm filter as a function of SED type. The three filters J, H and K are shown. The lower right plot shows the mean values for all three filters: solid: J, dashed: H, dotted: K. The crosses with the errorbars show the mean values and the variance in bins of 10 SED types.
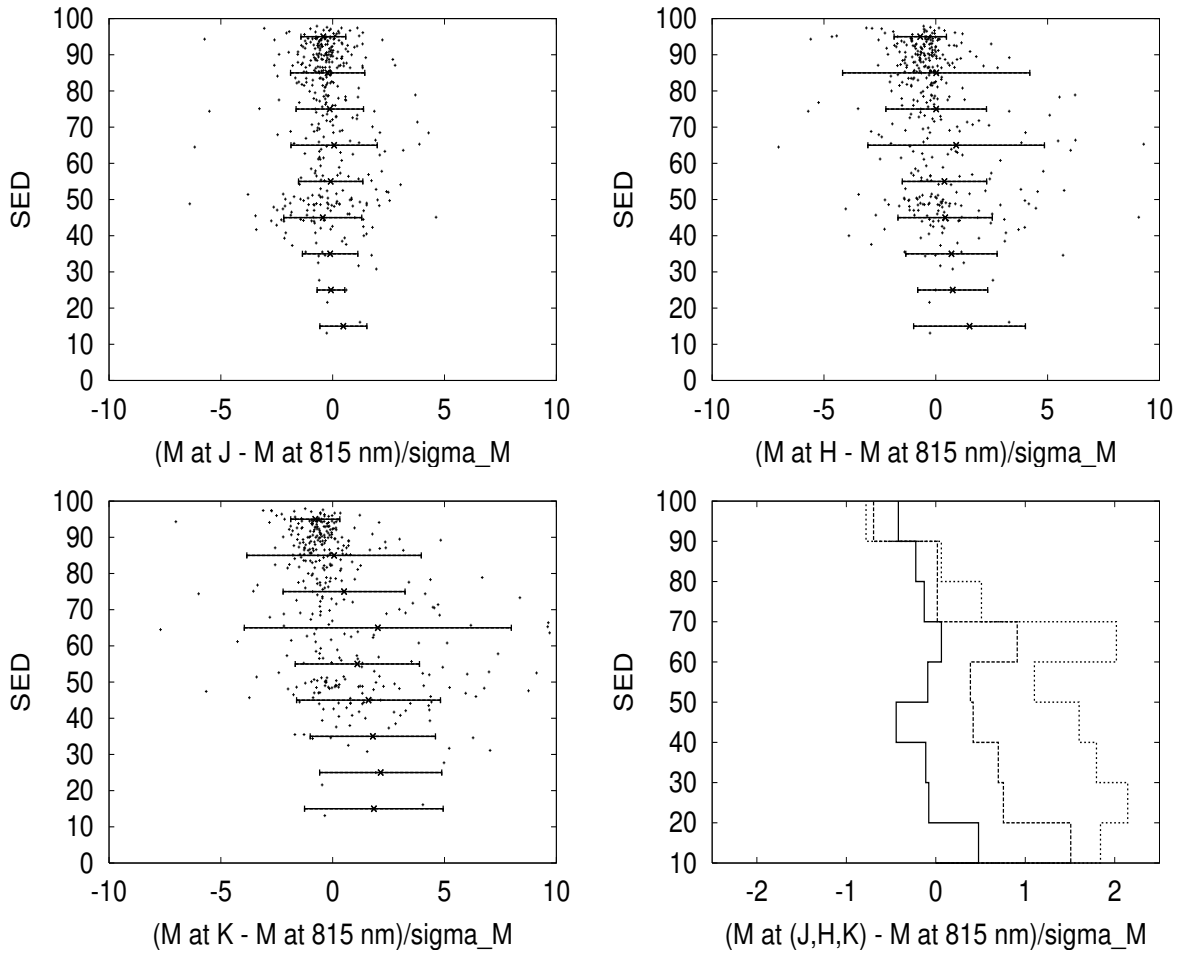
Figure 3.7: Difference between the stellar mass estimation in the infrared and the stellar mass estimation at the 815 nm filter divided by σ_M as a function of SED type. The three filters J, H and K are shown. The lower right plot shows the mean values for all three filters: solid: J, dashed: H, dottet: K. The crosses with the errorbars show the mean values and the variance in bins of 10 SED types.
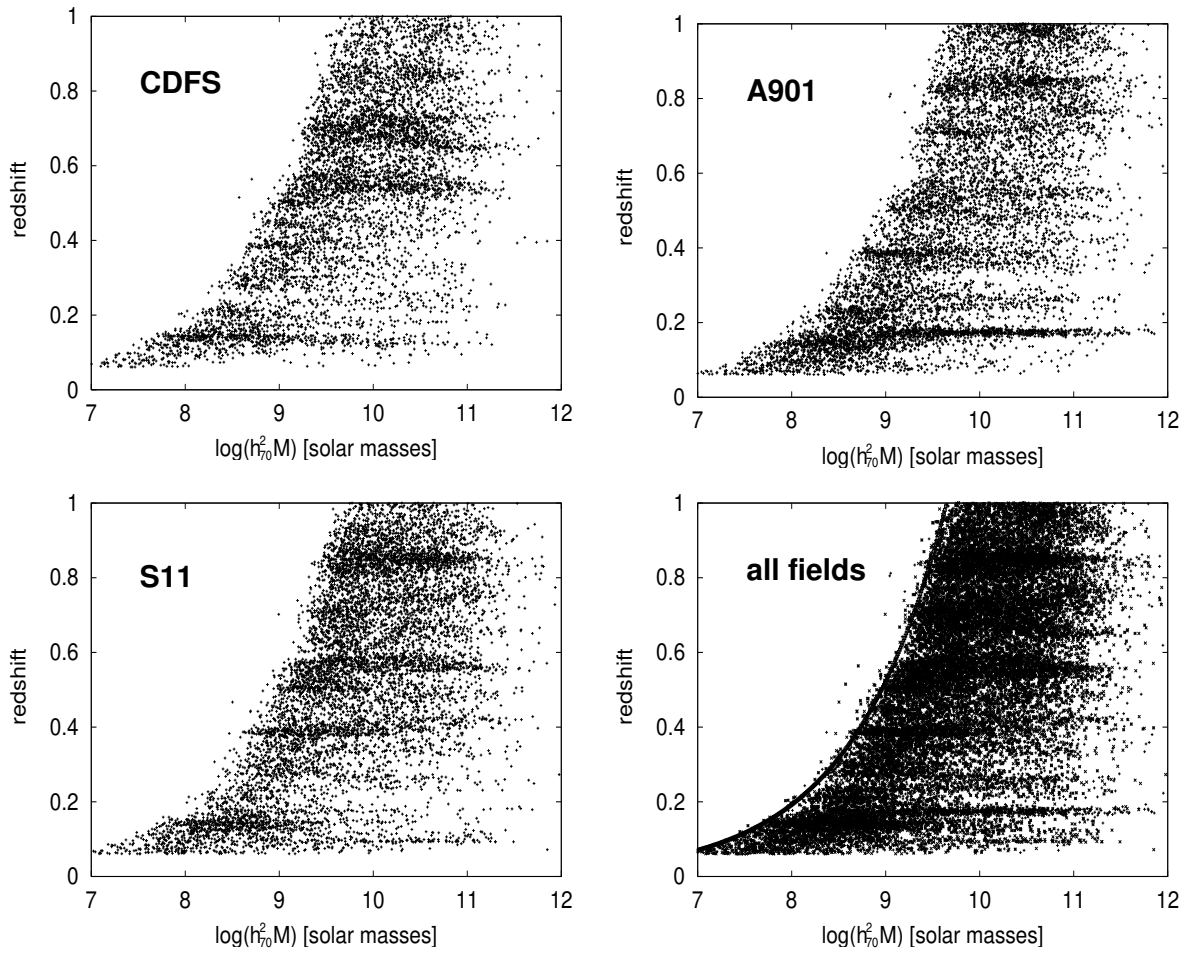
Figure 3.8: Stellar mass estimations vs. redshift. Three different COMBO-17 fields are shown. The lower right diagram shows the combination of all three fields. It also shows the function $z(M) = M^{\frac{1}{\ln(10)}}/15500$ which is a by eye fit to the left boundary.
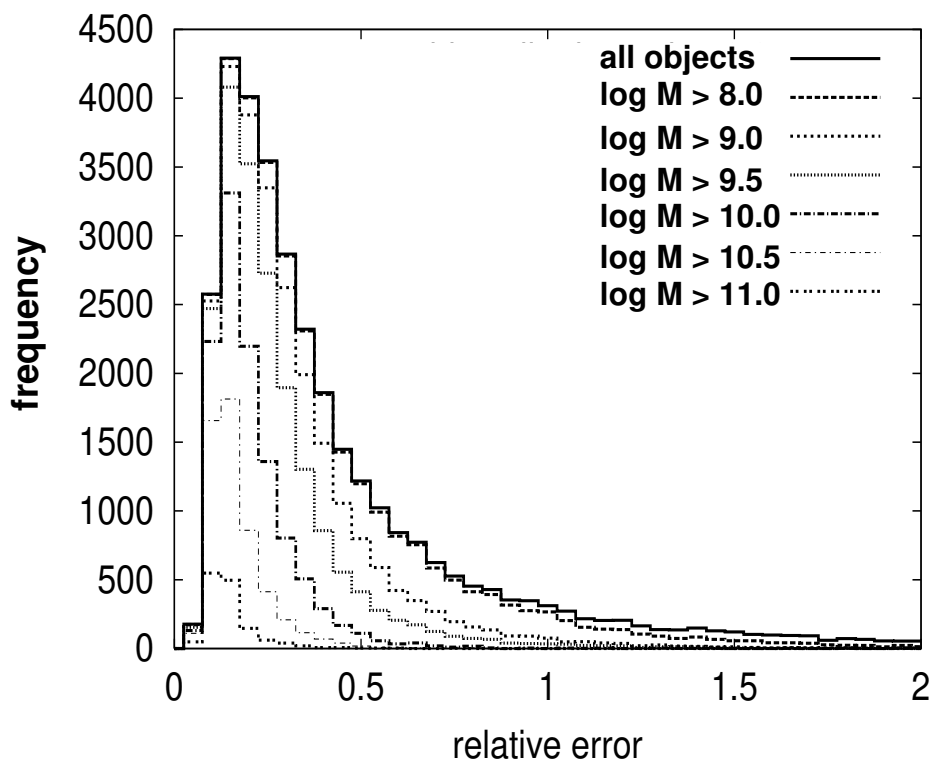
Figure 3.9: Relative errors of the stellar mass estimations for galaxies with different mass cuts.

Table 3.1: The parameters of the fits to the integrated stellar mass density as shown in figure 3.11. The fitted function is $\rho(z) = a \cdot z + b$. The table shows the parameters a and b for the fits including the SDSS value and without the SDSS value. The table also shows the mass increase factor $F = b/(a+b)$.

$\frac{M}{M_\odot}$	a $\left[\frac{M_\odot}{Mpc^3}\right]$	b $\left[\frac{M_\odot}{Mpc^3}\right]$	$\frac{b}{a+b}$
10^9	$-1.13 \pm 1.07 \cdot 10^8$	$3.23 \pm 0.42 \cdot 10^8$	1.54 ± 0.78
$10^{9.5}$	$-1.12 \pm 0.43 \cdot 10^8$	$3.13 \pm 0.24 \cdot 10^8$	1.55 ± 0.33
10^{10}	$-1.26 \pm 0.30 \cdot 10^8$	$3.05 \pm 0.19 \cdot 10^8$	1.71 ± 0.29
$10^{10.5}$	$-0.83 \pm 0.24 \cdot 10^8$	$2.41 \pm 0.15 \cdot 10^8$	1.52 ± 0.23
10^{11}	$0.05 \pm 0.22 \cdot 10^8$	$1.01 \pm 0.22 \cdot 10^8$	0.95 ± 0.20

$$
\begin{aligned}
V &= \frac{N}{4} \frac{square\,degree}{str} \cdot \int_{z1}^{z2} \frac{dV}{dz'\,d\Omega} dz' \\
&= \frac{N}{4} 3283 \frac{c}{H_0} \\
&\quad \cdot \int_{z1}^{z2} \frac{\frac{1}{(1+z')^2} D_L(z')^2\,dz'}{\sqrt{\Omega_M(1+z')^3 + \Omega_\lambda + (1-\Omega_M-\Omega_\lambda)(1+z')^2}}
\end{aligned}
\tag{3.11}
$$

Here N is the number of considered COMBO-17 fields (at the moment $N = 3$). D_L is the luminosity distance and z the redshift. For the cosmological parameters I use $\Omega_M = 0.3$ and $\Omega_\lambda = 0.7$. The redshifts z_1 and z_2 define a certain redshift interval that is considered. For example, the first plot in figure 3.10 considers the redshift interval $z_1 = 0.1$ to $z_2 = 0.25$ for which the volume V is calculated with this equation. The galaxies in the considered redshift bin and the considered mass bin are summed up and divided by V. The result is shown in figure 3.10 for six different redshift bins.

Figure 3.11 shows the integrated stellar mass density in galaxies at different mass cuts as a function of redshift. This means that only objects above the subsequent mass cut are considered. As a comparison, the zeropoints from the SDSS and 2MASS surveys from Bell et al. [2003] as plotted too. The offset between the SDSS value and the COMBO-17 data is due to the systematic mismatch of about 25%, as already seen in section 3.2.2. I correct this by shifting the SDSS value by 25%.

The parameters for a linear fit to the data is shown in table 3.1. I do not trust the last value due to the bad statistics when applying high mass cuts, above which only low object numbers show up.

Since the fitted function is $\rho(z) = a \cdot z + b$ the increasing factor of stellar mass since redshift 1 can be characterized by the value $F = \rho(z=0)/\rho(z=1) = b/(a+b)$. This value as a function of stellar mass cuts is plotted in figure 3.12. The average value for the stellar mass increase since redshift 1 is 1.6.

The local sample of galaxies is compared to the galaxies in the Abell 901 cluster. Figure 3.13 shows the stellar mass function in the Abell 901 cluster in comparison to the mass function in all three COMBO-17 fields at low redshifts. Above $3 \times 10^9 M_\odot$ the decrease is flatter in the cluster compared to the field and below this value the galaxies are less frequent than in the field.
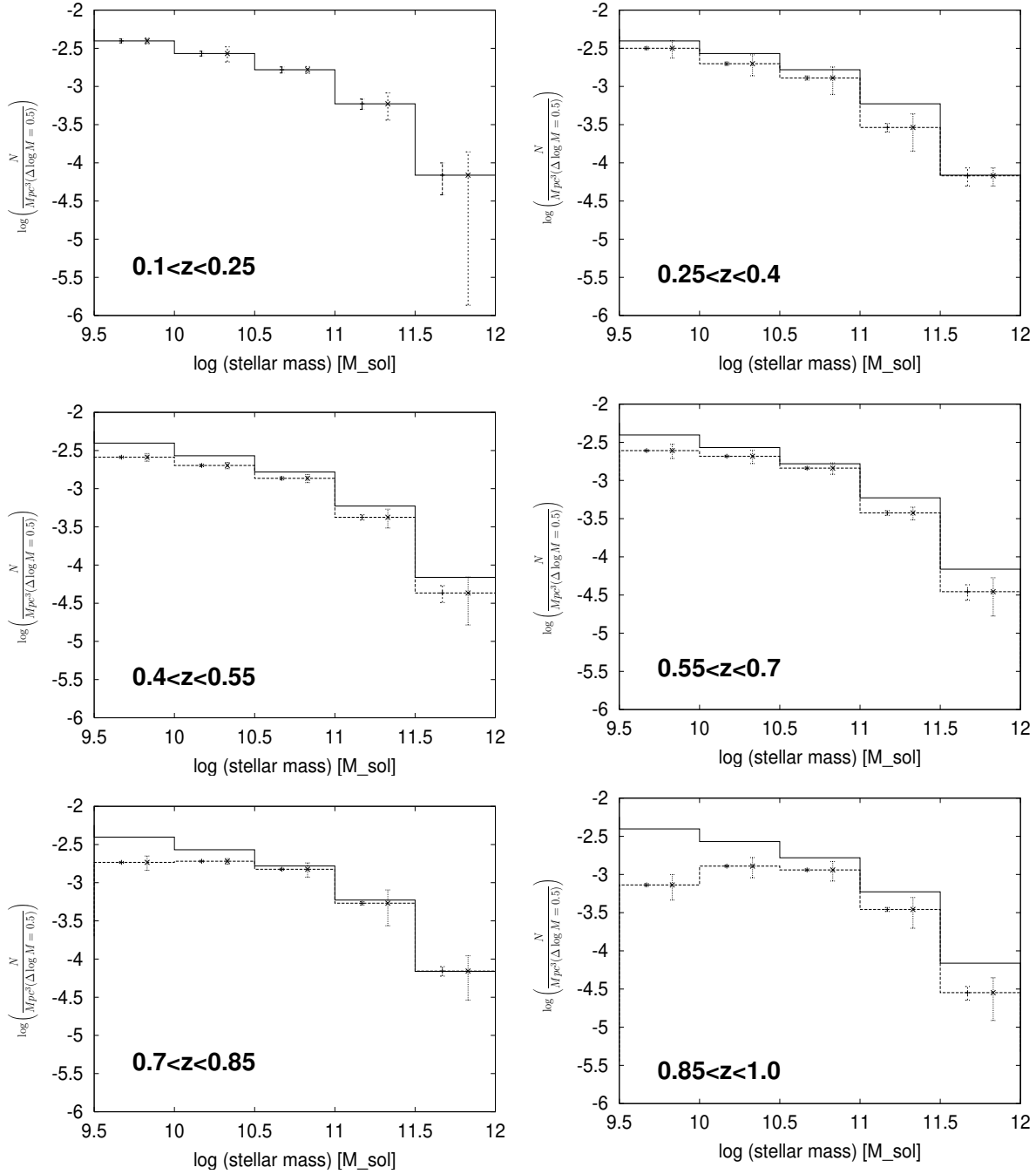
Figure 3.10: Stellar mass function per comoving volume at different redshift bins. The lowest redshift bin $0.1 < z < 0.25$ is shown in all plots as the solid histogram. The left errorbars in each bin show the statistical poisson errors and the right errorbars show the rms errors due to the field-to-field variation in the three COMBO-17 fields.
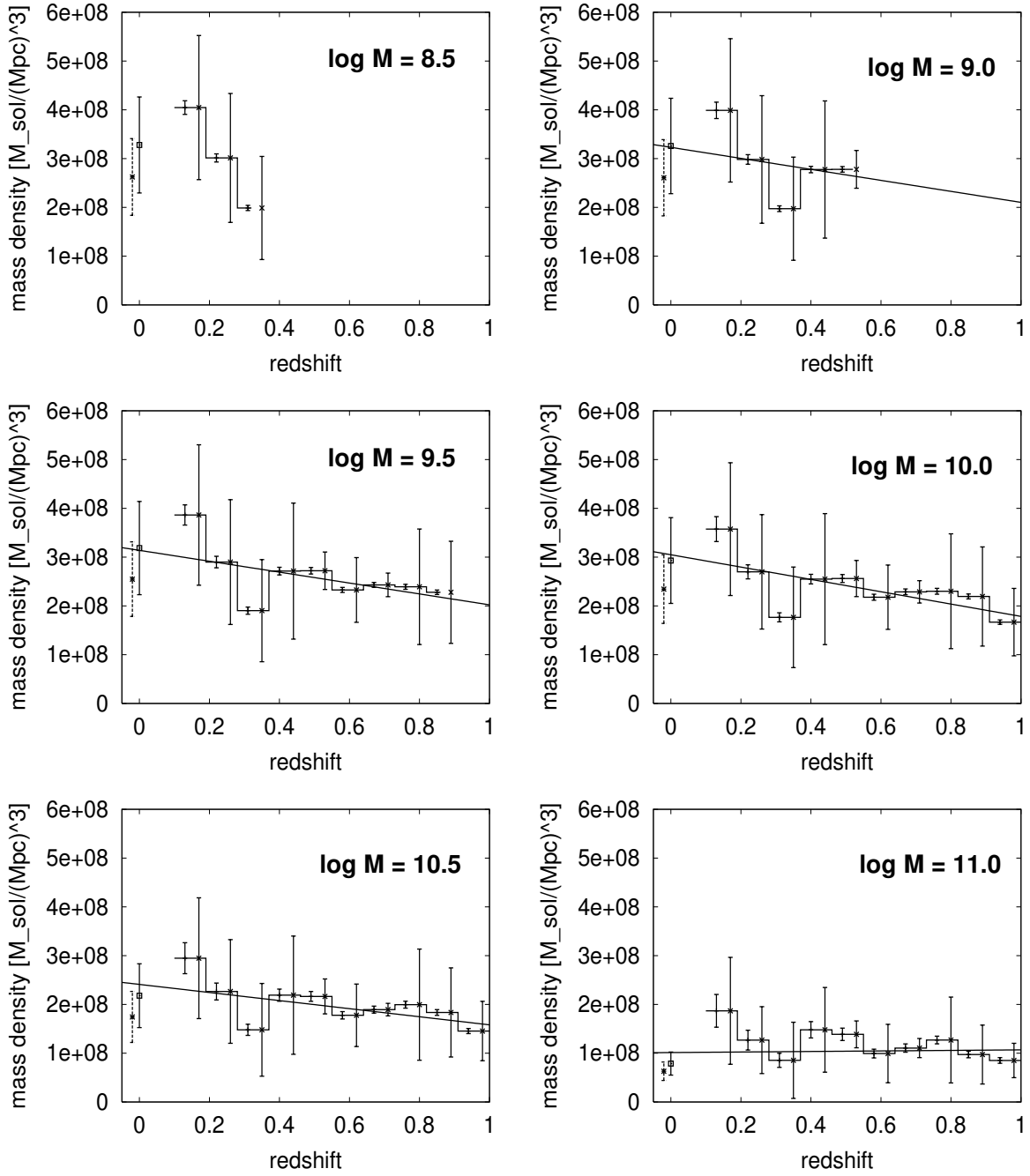
Figure 3.11: The integrated stellar mass density as a function of redshift with different mass cuts. Each of these plots shows the COMBO-17 result including all galaxies above a certain mass limit. The mass limit ranges from $M \geq 10^{8.5} M_\odot$ for the first plot to $M \geq 10^{11} M_\odot$ for the last plot. The histogram shows the mass density in galaxies per comoving $(Mpc)^3$. The zeropoints are the SDSS and 2MASS results from [Bell et al. 2003], calculated for the same mass cut. The dashed zeropoint is the original value and the solid zeropoint is offset corrected by 25 % by virtue of the systematic mismatch discussed in section 3.2.2. The left errorbars in each bin show the statistical Poisson errors and the right errorbars show the rms errors due to the field-to-field variation in the three COMBO-17 fields. The solid line is a least-square fit to the data.
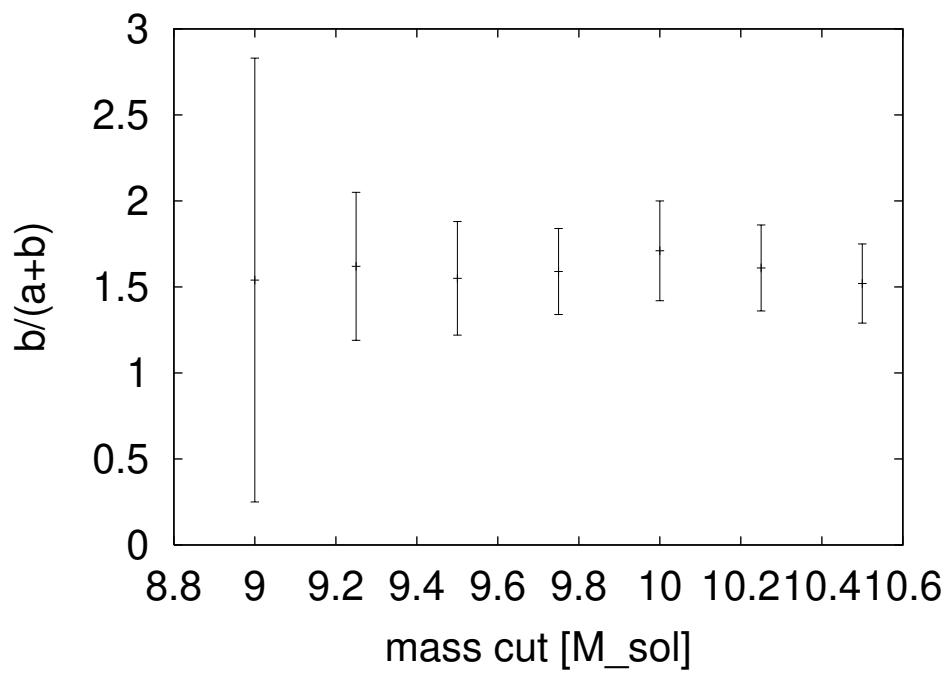
Figure 3.12: The increase of the integrated stellar mass density since redshift 1. The mass increase $F = b/(a + b)$ is plotted as a function of stellar mass cuts, above which the masses of the objects are taken into account.
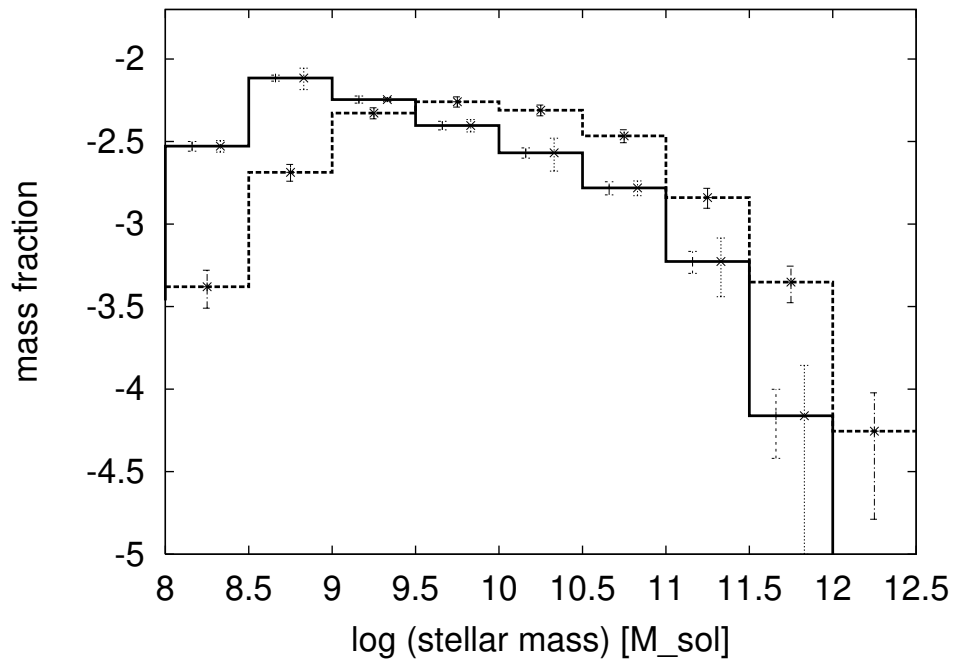
Figure 3.13: Stellar mass function per comoving volume at different redshift bins: solid: $0.1 < z < 0.28$ without the A901 galaxies, dashed: cluster galaxies at $0.15 < z < 0.2$ in the A901 field. The errorbars of the mass function without the A901 galaxies are the same as in figure 3.10. The errorbars of the cluster mass function are only the poisson errors.

Chapter 4

The piggyback method

As mentioned in section 2.6, the COMBO-17 team and the GEMS team use the J2003 library for the redshift and SED estimation. The F2003 library is better tailored to the stellar mass estimation. It is constructed making a suitable assumption for the properties of the underlying old stellar population contained in starburst galaxies. The J2003 library does not consider this. In order to take advantage of the improved redshifts in J2003 for the purpose of stellar mass estimation, I developed the piggyback method. It consists of two steps:

- Firstly the objects are classified by using the J2003 library. The redshifts from this classification are fixed in the following step.

- In the second step the SED type is classified again. The classification in this step is done by using the F2003 library.

With the aid of z from step 1 and SED from step 2 the stellar masses are estimated in the same way as described in chapter 3.

In order to test the code that is used for this purpose, I do firstly a selftest of this method. For that the objects are firstly classified with the F2003 library. The redshift is fixed at the so derived value and the objects are classified again with the same library. The difference to the method mentioned above is that also in the second step the F2003 library is used. The masses estimated with this selftest of the piggyback method are compared with the masses estimated with the F2003 classification, as described in chapter 3. The result of this comparison is shown in figure 4.1. As expected, the F2003 masses are reproduced well. The resulting mass deviations are caused by different results in the SED classification in the first and the second step. Figure 4.2 shows the SED deviations, this means the difference of the SED derived by the original F2003 classification and the SED derived in the second step. These SED deviations are caused by asymmetries in the probability distribution of the SED classification. Whereas the first classification takes place in the two-dimensional (SED,z) space, in the second step only the one-dimensional SED parameter is admitted as a free parameter. If the maximum of the probability distribution in the one-dimensional case is shifted with respect to the two-dimensional maximum, it leads to a different SED type.

In figure 4.3 the piggyback method is applied to the J2003 library. Compared to figure 4.1 it shows a stronger deviation. The comparison of the SED types is shown in figure 4.5. Here the difference of the F2003 SED's and the piggyback SED's is shown. A comparison to the J2003

SED's makes no sense because they are defined in a different way. Compared to the original F2003 mass estimation there is a scatter around zero, which is considerably higher than for the selftest.

The reason for the stronger SED scattering is that the redshifts in J2003 differ from those in F2003. The redshift difference is correlated to the SED difference. Figure 4.6 shows the SED difference in dependence of the redshift difference for different SED types. This correlation results from the connection shown in figure 3.1: The error estimation described in section 3.1.2 is similar to the selftest of the piggyback method described in this chapter. In the case of the error estimation the redshift is also fixed and the SED type is classified again. If the redshift is taken from J2003, the second classification delivers the SED type which is given by the correlation which is shown in figure 3.5. The correlation in figure 4.6 results from this.

The masses estimated by using the piggyback method are according to figure 4.3 different from the F2003 masses. The mass difference for the single object is caused by differences in the redshifts in J2003 and F2003. According to figure 4.6 this redshift difference causes derivations in the SED type, which cause derivations in the mass-to-light ratio. Since the factor $(1 = z)D_L^2$ goes down in equation (3.8), the redshift difference also causes directly a difference of the mass. As seen in chapter 2, the J2003 library delivers better redshift estimations. Therefore it is expected that the piggyback masses are more precise. In the statistical entirety these differences are a scattering around the zero line. Figure 4.4 shows the histogram of the differences of both masses. It is in the order of ± 0.1 dex.

Because the piggyback masses are consistent to the J2003 redshifts, the GEMS team and the COMBO-17 team use these masses. In the context of this work I do not use the piggyback masses on grounds of the self-consistence of the method of mass estimation described in chapter 3.
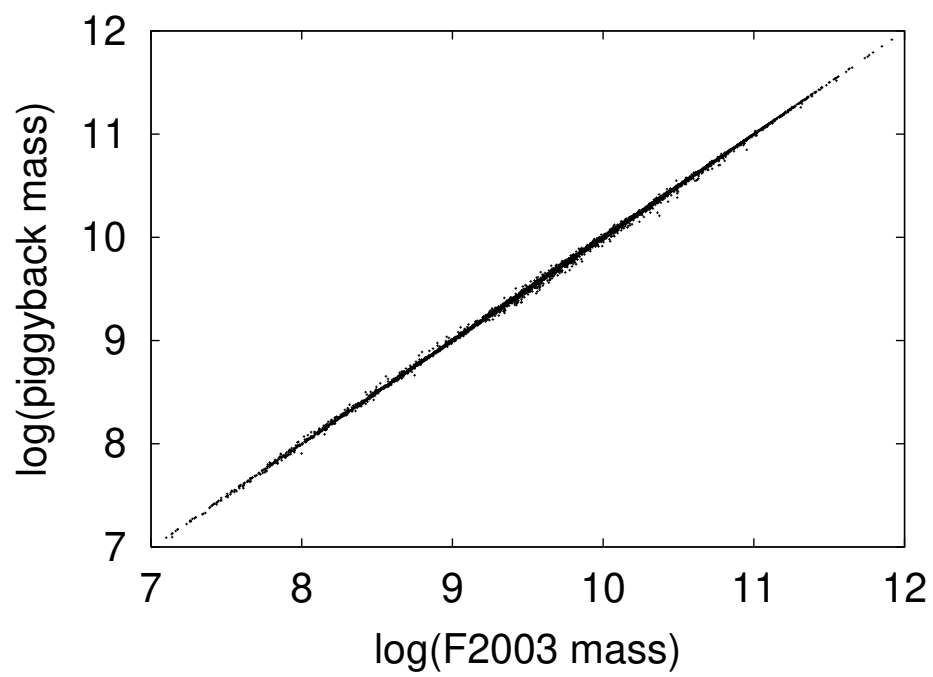
Figure 4.1: Comparison between the stellar masses derived with the F2003 library and the piggyback masses derived with the F2003 library. Since in both cases the same library is used, this is a selftest of the piggyback method.
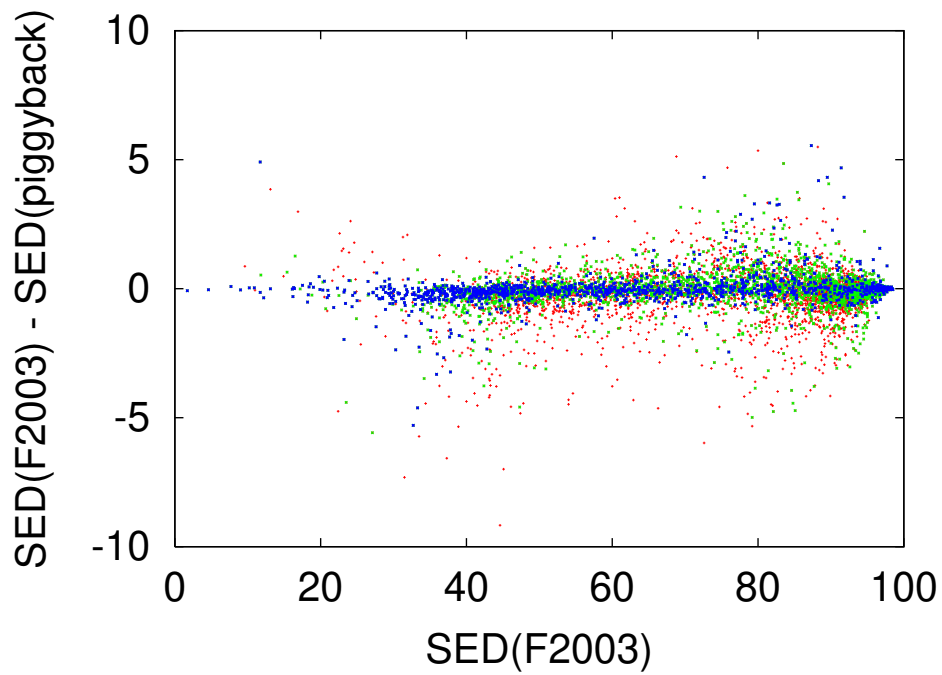
Figure 4.2: Comparison between the SED type derived with the F2003 library and the piggyback SED type derived with the F2003 library. Since in both cases the same library is used, this is a selftest of the piggyback method. Color coded are three limiting magnitudes: red: R≤24, green: R≤23, blue: R≤22
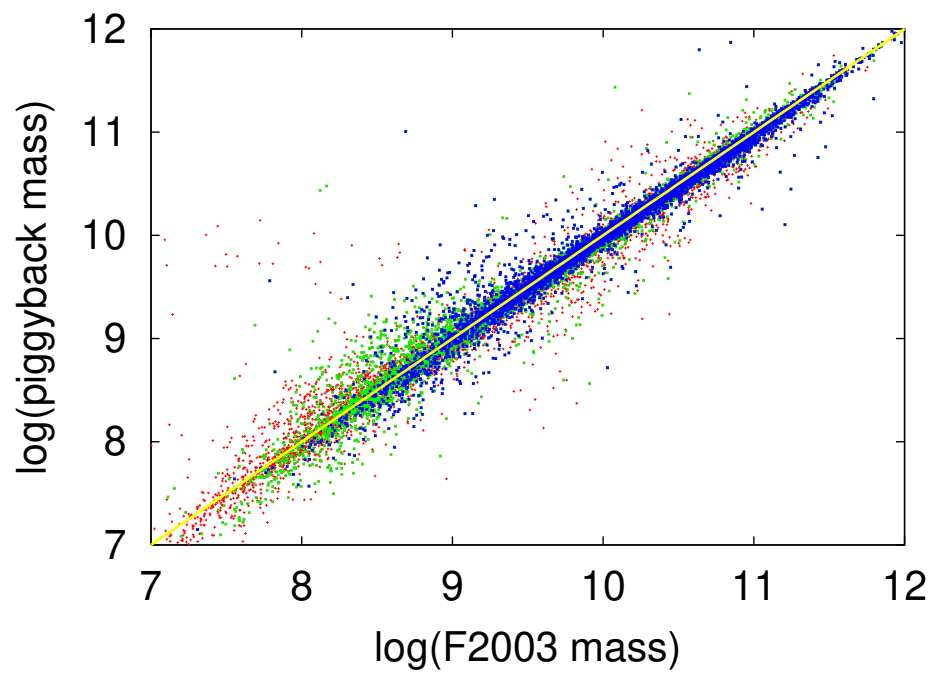
Figure 4.3: Comparison between the stellar masses derived with the F2003 library and the piggyback masses derived with the J2003 library. Color coded are three limiting magnitudes: red: R≤24, green: R≤23, blue: R≤22
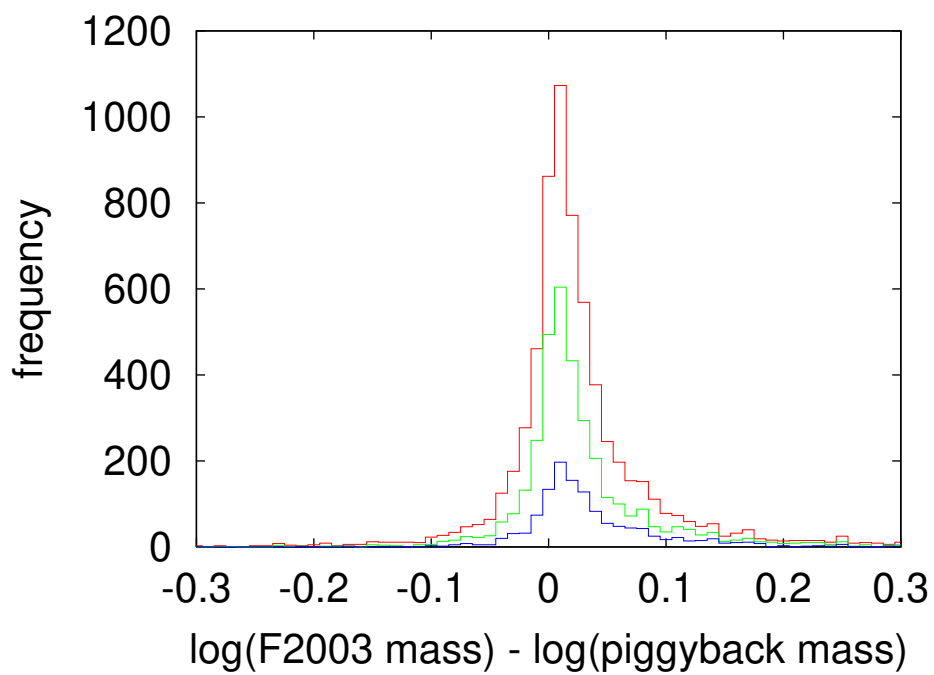
Figure 4.4: Histogram of the differences between the stellar masses derived with the F2003 library and the piggyback masses derived with the J2003 library, as seen in figure 4.3. Color coded are three limiting magnitudes: red: R≤24, green: R≤23, blue: R≤22
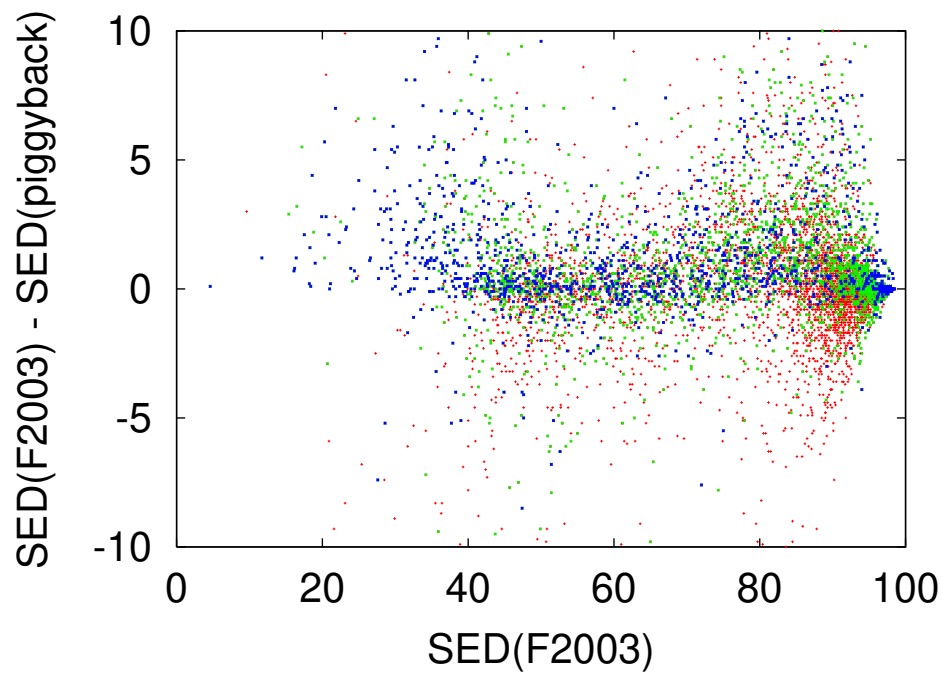
Figure 4.5: Difference between the SED type derived with the F2003 library and the piggyback SED type derived with the J2003 library as a function of SED type. Color coded are three limiting magnitudes: red: R≤24, green: R≤23, blue: R≤22
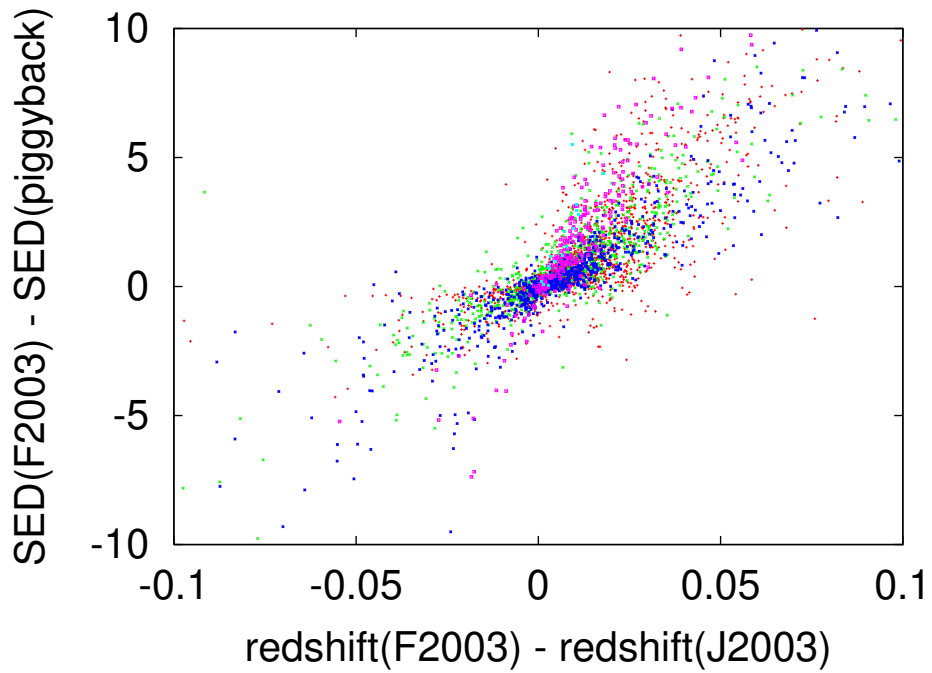
Figure 4.6: Correlation between the redshift difference and the SED type difference. The x-axis shows the difference between the redshifts derived from classifications with the J2003 library and the F2003 library. The y-axis shows the difference between the SED classification with the piggyback method and the SED classification with the F2003 library. Color coded are different regimes of SED types: red:$80 \leq SED \leq 100$, green:$60 \leq SED \leq 80$, blue:$40 \leq SED \leq 60$, purple:$20 \leq SED \leq 40$, light blue:$1 \leq SED \leq 20$,

Chapter 5

Discussion

In this section the redshift evolution ot the integrated stellar mass density (figure 3.11) is discussed, which is the main result of this work. As seen in figure 3.12, there is an average increase of the stellar mass density of a factor of F = 1.6. This means that at the present epoch there is about 1.6 times more stellar mass in galaxies than at redshift 1. In more detail, the stellar mass density is about $2 \times 10^8 M_\odot/Mpc^3$ at redshift 1 and about $3 \times 10^8 M_\odot/Mpc^3$ at redshift 0 for mass cuts $M \leq 10^{10} M_\odot$ (see figure 3.11). In the following it is discussed how does this result compare to the semianalytic model, to results of other surveys and to the integrated star formation rate.

For the comparison to the semianalytic models I use a mass cut of $M \geq 10^{10} M_\odot$ (see figure 3.11) in order to avoid completeness issues in the sense that at all redshifts this mass cut is above the solid line in figure 3.8. The result for this mass cut is compared to the semianalytic models of R. Somerville [Somerville & Primack 1999] and Cole et al. [Cole et al. 2000], which is shown in figure 5.1. The semianalytic models are described briefly in section 1.1 in the introduction. The result of the model of R. Somerville (priv. comm.) agrees both in the absolute calibration and in the slope. For the result I obtained from C. Baugh (priv. comm.) only the slope can be compared, whereas the absolute value is suitable normalized. The result of the F = 1.6 increase in mass density since redshift 1 as mentioned above is in good agreement to the semianalytic model of R. Somerville which predicts an increase of 1.75 since redshift 1. The semianalytic model of C. Baugh et al. predicts a slightly higher factor of 1.9. Whereas these models have already been compared to the mass increase expected from the integrated Madau plot (R. Somerville, priv. comm.), our result is another independent test for these models.

The COMBO-17 result is compared to the FIRES result [Rudnick et al. 2003] and also to the MUNICS result [Drory et al. 2004]. In [Rudnick et al. 2003] the results of different surveys are summarized. Figure 5.2 shows the integrated stellar mass density for the luminosity cut $L_V^{rest} > 1.4 \times 10^{10} h_{70}^{-2} L_{V,\odot}$ which is chosen in order to be consistent to figure 8 of [Rudnick et al. 2003]. Whereas in this work I use an IMF of Kroupa et al. [1993], Rudnick et al. use a Salpeter IMF. In [Bell et al. 2003] a conversion factor of 0.25 dex between these two IMF's is given. This is used here in order to transform the results in figure 8 of [Rudnick et al. 2003] to a Kroupa IMF. In addition, the 0.1 dex mismatch, as already seen in section 3.2.2 is taken into account. Therefore, rather a conversion factor of 0.15 dex is used here. The other survey results shown in figure 8 of [Rudnick et al. 2003] are repeated in figure 5.2. This comparison shows an
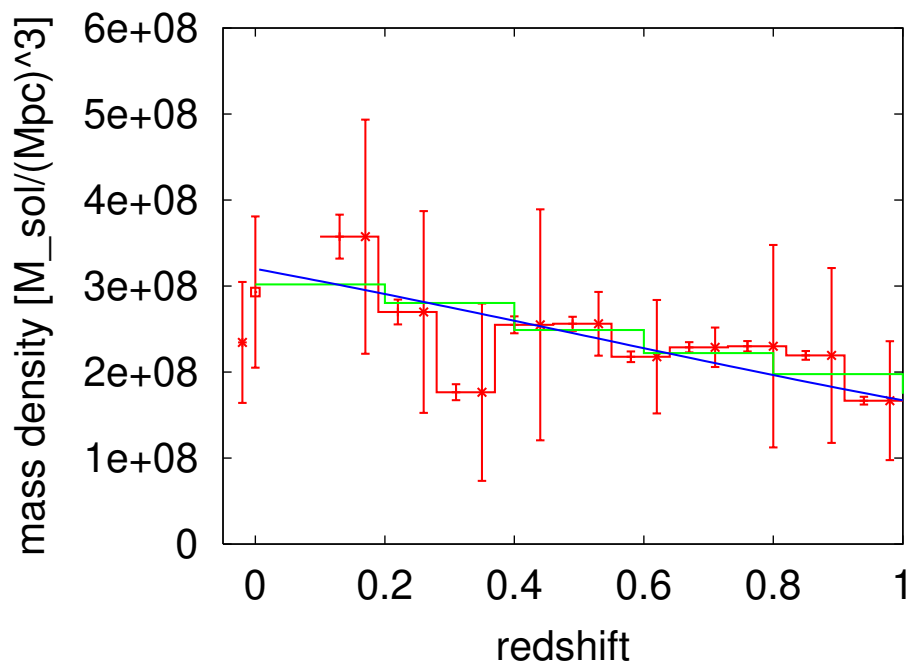
Figure 5.1: Comparison to the results of the semianalytic models of R. Somerville and C. Baugh et al.. The red histogram is the same plot as shown in figure 3.11 for a cutoff mass of $10^{10} M_\odot$. This is compared to the semianalytic models of R. Somerville (green histogram) and C. Baugh et al. (blue line), which is suitably normalized.
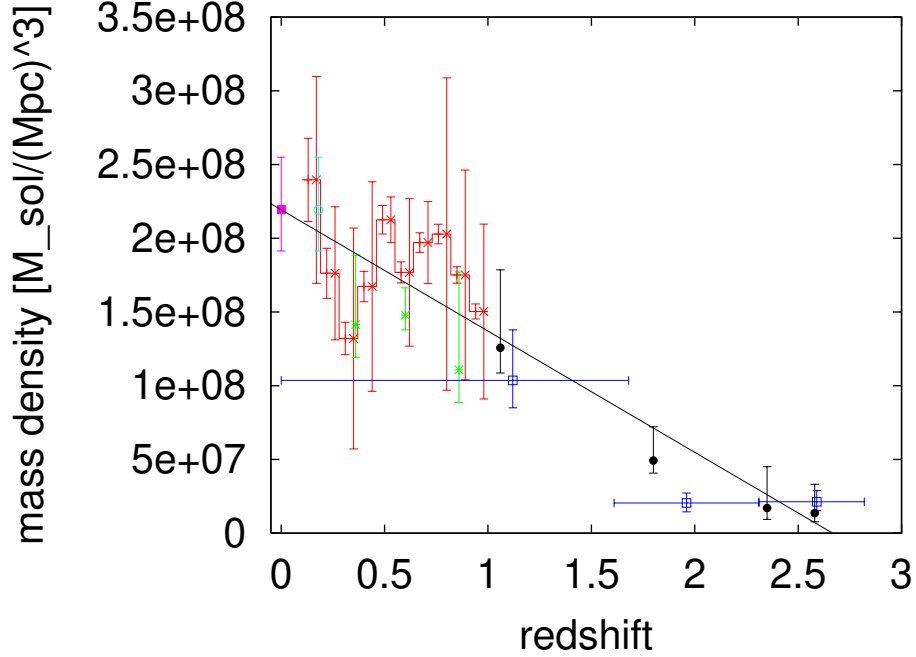
Figure 5.2: The COMBO-17 result in comparison to the results of other surveys, which are taken from figure 8 in [Rudnick et al. 2003]. In order to be consistent to this work, a mass cut of $L_V^{rest} > 1.4 \times 10^{10} h_{70}^{-2} L_{V,\odot}$ is used. Color coded are shown different surveys: red: COMBO-17, green:CFRS, bue: FIRES, purple: 2dGRS+2MASS, light blue: SDSS, black: HDF-N. The refrerences for these survey results are given in [Rudnick et al. 2003]. The errorbars of the COMBO-17 results are both the statistical Poisson errors (left errorbars) and the rms-errors due to field-to-field variation (right errorbars). The black line shows the F=1.6 slope, which is the COMBO-17 result for the stellar mass increase since redshift 1.

overall picture up to redshift 3, which is consistent to the aforementioned F = 1.6 factor for the stellar mass increase since redshift 1, as shown as the black line in figure 5.2.

In figure 5.3 the comparison to the MUNICS result is shown. Drory et al [2004] found a stellar mass increase by a factor of 2 since redshift 1, which is a little bit higher than the F = 1.6 value from COMBO-17. They analysed a field of 0.28 square degree, which corresponds to one COMBO-17 field. Since they use a Salpeter IMF I apply again the 0.15 dex conversion factor to the MUNICS result. The absolute calibration of the MUNICS result shows a systematic mismatch compared to the COMBO-17 result.

The COMBO-17 result is compared to the integrated star formation rate [Madau et al. 1996]. In figure 12 in [Hippelein et al. 2003], which is repeated in figure 1.3 in the introduction, the dashed line shows the power law

$$SFR \propto \exp\left(\frac{t_{lookback}}{2.6\,Gyr}\right) \tag{5.1}$$

for redshifts below ≈ 1.0 with a value around $0.155 M_\odot Mpc^{-3} yr^{-1}$ at redshift 1.0. These values predict a stellar mass density at redshift 1 and redshift 0 just by integrating the star formation
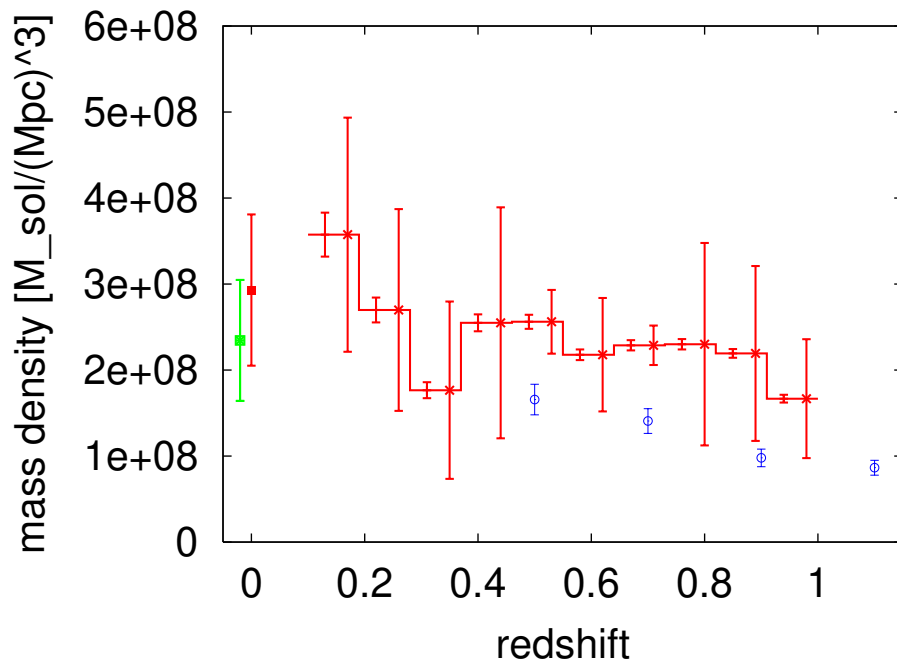
Figure 5.3: Comparison to the MUNICS result [Drory et al. 2004]. The red histogram is the same plot as shown in figure 3.11 for a cutoff mass of $10^{10} M_\odot$, which is the same mass cut as used in [Drory et al. 2004].This is compared to the MUNICS result of the integrated stellar mass density (blue points).

Table 5.1: The star formation rate of [Hippelein et al. 2003] integrated over the lookback time in comparison to the COMBO-17 result of the integrated stellar mass density. The "pure integration" neglects mass loss, whereas the integration by using the PEGASE code calculates this mass loss intrinsically.

	pure integration	PEGASE	COMBO-17 result
$z = 1.0$	$9.6 \cdot 10^8 M_\odot Mpc^{-3}$	$7.9 \cdot 10^8 M_\odot Mpc^{-3}$	$2 \times 10^8 M_\odot / Mpc^3$
$z = 0.0$	$14.1 \cdot 10^8 M_\odot Mpc^{-3}$	$10.75 \cdot 10^8 M_\odot Mpc^{-3}$	$3 \times 10^8 M_\odot / Mpc^3$
F	1.4	1.34	1.6

rates over the lookback time. Integrating the SFR of $0.155 M_\odot Mpc^{-3} yr^{-1}$ from $z = \infty$ to $z = 1$ leads to a mass density of $9.6 \cdot 10^8 M_\odot Mpc^{-3}$ at redshift 1. This is done under the assumption that the SFR is a constant in this time interval. In the redshift regime $0 \leq z \leq 1$ the integration of power law (5.1) delivers a value of $4.1 \cdot 10^8 M_\odot Mpc^{-3}$. Hence, these two values give a stellar mass increase of F = 1.4, which is a slightly lower value than the F = 1.6 factor of the COMBO-17 result.

However, this integration neglects any mass loss due to supernova events which remove stellar mass. In order to take this mass loss into account, the same star formation rates are applied to the PEGASE code, which assumes this mass loss intrinsically. Feeding the PEGASE code with a constant SFR of $0.155 M_\odot Mpc^{-3} yr^{-1}$ and running the code over the lookback time in the interval $1 \leq z \leq \infty$ delivers a stellar mass density of $7.9 \cdot 10^8 M_\odot Mpc^{-3}$ at $z = 1$. Applying the star formation history (5.1) to the code and run over the interval $0 \leq z \leq 1.0$ leads to a value of $2.85 \cdot 10^8 M_\odot Mpc^{-3}$. For these values the stellar mass increase factor is F = 1.34. Compared to the value derived by simple calculation there is a mass loss of 18 % in the redshift interval and of 30 % in the redshift interval $0 \leq z \leq 1$.

Table 5 summarizes the results. Whereas the increasing factor F is in consideration of the errors consistent with the COMBO-17 data, the absolute values of the integrated stellar mass are by far too high. The $z = 1$ value is 5 times higher than the COMBO-17 result in the case of pure integration and 4 times higher in the PEGASE case, where the mass loss is taken into account. At $z = 0$ the pure integration value is 4.6 times higher and the PEGASE value 3.6 times higher than the COMBO-17 result.

In summary, the values delivered by the integration over the Madau plot are too high, but the observation of the mass increase since redshift 1.0 seems to be consistent with the star formation rate in the same redshift regime. The factor 4-5 mismatch until redshifts 1.0 may reflect uncertainties in the initial mass function. Whereas the measurements of star formation rates rely in particular on high mass stars, the stellar mass estimation in this work relies in particular on stars with masses around $1 M_\odot$ or even lower. Hence, drawing integrated stellar mass densities in galaxies just by integrating the Madau plot may deliver a somewhat misleading picture. At the high mass end, some initial mass functions agree, and therefore the high mass stars are not sensitive to distinguish between different IMF's. For example, the Kroupa IMF and the Salpeter IMF are basically the same at the high mass end. Whereas the high mass stars show more the "tip of the iceberg", the mass region around 1 $M_\odot$ is more typical for the stellar

population. Therefore it is important to have a good assumption of the low-mass end of the IMF. Bell & de Jong [2001] have demonstrated that different IMF assumptions cause different calibrations in the stellar mass-to-light ratios. Even when I apply the above used conversion factor between a Kroupa IMF and a Salpeter IMF to the integrated star formation rates, there remains a mismatch to the COMBO-17 result. Maybe this reflects, that the Kroupa IMF, which is used in this work is not a good assumption. One possible explanation is that the assumption of an unique IMF that is basically measured in the Galaxy is a too simple extrapolation to galaxies at higher redshifts.

On the other hand, [Rudnick et al. 2003] argue that their result is consistent to the integral of the SFR of Cole et al. [2001], which is for the $E_{B-V} = 0.15$ case basically identical to figure 12 in [Hippelein et al. 2003]. They apply to the stellar mass densities at their V-band luminosity cut a factor of 2 correction to the total stellar mass by using the low-redshift stellar mass function from 2MASS. When looking to the stellar mass functions as shown in figure 3.10 I cannot confirm this factor of 2 correction to the total stellar mass density. For $z = 0$ they end up with a total stellar mass density of $6 \times 10^8 M_\odot/Mpc^3$ and about $6 \times 10^8 M_\odot/Mpc^3$ at $z = 1$. Hence, compared to the calculation shown above there is still a factor of 2 missing, even when one accepts the factor 2 correction.

I also investigated the galaxies in the Abell 901 cluster and compared this result with the field galaxies. As seen in figure 3.13, the cluster galaxies contain on average more mass than the field galaxies. This might reflect the fact that in the dense cluster environment where the mass assembly due to mergers is more common than in the field, under the assumption that the stellar mass would be a proxy for the total mass of a galaxy in some sense. Another (perhaps more likely) interpretation is that in cluster galaxies the star formation started earlier and therefore the stellar populations are older than in field galaxies. In this case there was more time to build up stellar mass.

Chapter 6

Outlook

6.1 Evolution of the galaxy population from z=1 to today

The COMBO-17 dataset with its stellar mass estimation allows an investigation of the data cube spanned by the parameters stellar mass, (U-B) color and redshift. The modeling of simple stellar populations and simple approaches to the evolution of galaxies can be used to investigate evolutionary tracks of different galaxy types in this data cube. Such an investigation is similar to the evolutionary tracks of stars in the Hertzsprung-Russel diagram.

Monte Carlo simulations would allow to investigate the galaxy density at each point in this data cube. Normalized to the local value of the mass distribution of galaxies obtained from SDSS data by [Kauffmann et al. 2003] the galaxy density in the data cube is predictable for different approaches to explain the evolution of galaxies. This can be compared to the COMBO-17 data in order to constrain possible assumptions.

6.2 The actual star formation rate of galaxies

The philosophy of using the SED and redshift estimation from multi-color surveys like COMBO-17 by using a galaxy template library based on stellar population synthesis modeling is an ideal tool not only for estimating the stellar masses but also for estimating the actual star formation rate of starburst galaxies. Whereas for the purpose of stellar mass estimations the infrared regime is most interesting in order to trace the old stellar population, for the SFR estimations it is the UV regime. In this wavelength region the young stars dominate the light of the galaxy. In order to avoid uncertainties concerning the IMF the best way of estimating the SFR is to measure the UV fluxes. At higher redshifts the UV flux is shifted more and more into the optical and thus observable from the ground. For low redshifts the UV images have to be taken in space. Furthermore, the galaxy template library needs to be reliable in the UV regime. Up to now, the PEGASE library is designed such that it matches the Kinney et al. templates. However, in the UV region their reliability remains to be further investigated. This concerns not only the galaxy templates but also the stellar libraries in the stellar population synthesis models itself. Both is expected to be improved in the near future due to advanced measurements in the UV regime as well as improvements in the stellar population synthesis modeling.

6.3   Baryonic and dark matter

Rocca-Volmerange et al. [2004] demonstrated the estimation of the baryonic mass of the initial gas halo from which the gas flows into the central part and forms a galaxy. They derived a maximal baryonic mass of 10^{12} solar masses for a sample of radio loud galaxies of De Breuck et al. [2002], which is similar to the critical mass of a self-gravitating cloud regulated by cooling (Rees & Ostriker 1977). This can be verified with the larger sample of COMBO-17.

The PEGASE code allows to transform the stellar mass estimations into these initial baryonic masses. Therefore these two parameters can be linked together for a given SED type. Since the SED type is estimated for each galaxy, this would lead to an initial baryonic mass estimation. For this purpose the star formation histories of the template library galaxies, which are so far modeled by the assembly of three different components have to be replaced by one single component that describes the evolution in a more self-consistent manner.

One possible application may be the comparison of the integrated baryonic mass of the Abell 901 galaxy cluster to the total mass of this of this cluster, derived by M. Gray by using lensing techniques. This would enable an investigation of the dark matter content.

Bibliography

[Bell & de Jong 2001] Bell, E.F., de Jong, R.S., ApJ 550, 212 (2001)

[Bell et al. 2003] Bell, E.F., McIntosh, D.H., Katz, N., Weinberg, M.D, ApJS 149, 289-312 (2003)

[Binggeli et al. 1988] Binggeli, B., Sandage, A., Tammann, G.A., ARAA 26, 509-560 (1988)

[Binney & Merrifield 1998] Binney, J., Merrifield, M., Galactic Astronomy, Princeton University Press 1998

[Borch et al. 2003] Borch A., Meisenheimer K., Wolf C., Gray M., Ap&SS 284, 965-968 (2003)

[De Breuck et al. 2002] De Breuck, C., van Breugel, W., Stanford S.A. et al., AJ, 123, 637 (2002)

[Broadhurst et al. 1992] Broadhurst, T.J., Ellis, R.S., Glazebrook, K. Nature 355, 55-58 (1992)

[Bruzual & Charlot 1993] Bruzual, G., Charlot, S., ApJ 405, 538-553 (1993)

[Bruzual & Charlot 2003] Bruzual, G., Charlot, S., MNRAS 344, 1000-1028 (2003)

[Clemens et al. 1985] Clemens, D.P., ApJ 295, 422-436 (1985)

[Cole et al. 2000] Cole, S., Lacey, C.G., Baugh, C.M., Frenk, C.S., MNRAS 391, 168-204 (2000)

[Cole et al. 2001] Cole, S., Norberg, P., Baugh, C.M. et al., MNRAS 326, 255-273 (2001)

[Dekel & Silk 1986] Dekel, A., Silk, J., ApJ 303, 39-55 (1986)

[Drory et al. 2003] Drory, N., Bender, R., Feulner, G., Hopp, U., Marastron, C., Snigula, J., Hill, G.J., ApJ 595, 698-711 (2003)

[Drory et al. 2004] Drory, N., Bender, R., Feulner, G., Hopp, U., Marastron, C., Snigula, J., astro-ph/0403041

[Fried et al. 2001] Fried, J.W., von Kuhlmann, B., Meisenheimer, K., Rix, H.-W., Wolf, C., Hippelein, H.H., Kümmel, M., Phleps, S., Röser, H.J., Thierring, I., Maier, C., A&A 376, 788-800 (2001)

[Guiderdoni & Rocca-Volmerange 1987] Guiderdoni, B., Rocca-Volmerange, B., A&A 186, 1-21 (1987)

[Hatziminaglou et al 2002] Hatziminaglou, E., Groenewegen, M.A.T., da Costa, L. et al., astro-ph/0201028

[Hippelein et al. 2003] Hippelein, H., Maier, C., Meisenheimer, K., Wolf, C., Fried, J.W., von Kuhlmann, B., Kümmel, M., Phleps, S., Röser, H.-J., A&A 402, 65 (2003)

[Kauffmann & Charlot 1998] Kauffmann, G. Charlot, S., MNRAS 297, L23-L28 (1998)

[Kauffmann et al. 2003] Kauffmann, G., Heckmann, T.M., White S.D.M. et al.; MNRAS 341, 33-53 (2003)

[Kinney et al. 1996] Kinney, A.L., Calzetti, D., Bohlin, R.C., McQuade, K., Storchi-Bergmann, T., Schmitt, H.R., ApJ 467, 38 (1996)

[Fioc & Rocca-Volmerange 1997] Fioc, M., Rocca-Volmerange, B., A&A 326, 950 (1997)

[Kochanek et al. 2001] Kochanek, C. S., Pahre, M. A., Falco, E. E., Huchra, J. P., Mader, J., Jarrett, T. H., Chester, T., Cutri, R., Schneider, S. E., ApJ 560, 566 (2001)

[Kroupa et al. 1993] Kroupa, P., Tout, C.A., Gilmore, G., MNRAS 262, 545-587 (1993)

[Lilly et al. 1995] Lilly, S.J., Tresse, L., Hammer, F., Crampton, D., Le Fevre, O., ApJ 455, 108-124 (1995)

[Madau et al. 1996] Madau, P., Ferguson, H.C., Dickinson, M.E., Giavalisco, M., Steidel, C.C., Fruchter, A., MNRAS 283, 1388-1404 (1996)

[Matteucci 2003] Matteucci F., Ap&SS 284, 965-968 (2003)

[Méra et al. 1998] Méra, D., Chabrier, G., Schaeffer R., A&A 330, 937-952 (1998)

[Mouhcine & Lançon 2003] Mouhcine, M., Lancon, A., A&A 402, 425-432 (2003)

[Pagel 1997] Pagel B.E.J. Nucleosynthesis and Chemical Evolution of Galaxies, Cambridge University Press 1997

[Pozzenti et al. 2003] Pozzetti, L., Cimatti, A., Zamorani, G., Daddi, E., Menci, N., Fontana, A., Renzini, A., Mignoli, M., Poli, F., Saracco, P., Broadhurst, T., Cristiani, S., D'Odorico, S., Giallongo, E., Gilmozzi, R., A&A 402, 837-848 (2003)

[Press & Schechter 1974] Press, W.H., Schechter, P., ApJ 187, 425-438 (1974)

[Rees & Ostriker 1977] Rees, M.J., Ostriker, J.P., MNRAS 179, 541-559 (1977)

[Rix et al. 2004] Rix, H.-W., Barden, M., Beckwith, S.W.V., Bell, E.F., Borch, A., Caldwell, J.A.R., Häußler, B., Jahnke, K., Joggee, S., McIntosh, D.H., Meisenheimer, K., Peng, C.Y., Sanchez, S.F., Somerville, R.S., Wisotzki, L., Wolf, C., ApJSS 152 (2), 163-173 (2004)

[Rocca-Volmerange et al. 2004] Rocca-Volmerange, B., Le Borgne, D., De Breuck, C., Fioc, M., Moy, E., A&A 415, 931-940 (2004)

[Rudnick et al. 2003] Rudnick, G.,Rix, H.-W.,Franx, M., Labbé, I., Blanton, M., Daddi, E., Förster-Schreiber, N., Moorwood, H., Trujillo, I., van de Wel, A., van den Werf, P., van Dokkum, P., van Starkenburg, L., ApJ 599, 847-864 (2003)

[Somerville & Primack 1999] Somerville, R. S., Primack, J. R., MNRAS 310, 1087-1110 (1999)

[Tinsley 1972] Tinsley, B.M., A &A 20, 383–396 (1972)

[Toomre & Toomre 1972] Toomre, A., Toomre, J., ApJ 178, 623-666 (1972)

[Wolf, PhD thesis] Wolf C., PhD thesis, Universität Heidelberg (1999)

[Wolf et al. 2001a] Wolf, C., Meisenheimer, K., Röser, H.-J., Beckwith, S.V.W., Chaffee, F.H., Fried, J., Hippelein, H., Huang, J.-S., Kümmel, M., von Kuhlmann, B., Maier, C., Phleps, S., Rix, H.-W., Thommes, E., Thompson, D., A&A 365,681–698 (2001)

[Wolf et al. 2001b] Wolf, C., Meisenheimer, K., Röser, H.-J., A&A 365, 660 (2001)

[Wolf et al. 2003] Wolf, C., Meisenheimer, K., Rix, H.-W., Borch, A., Dye, S., Kleinheinrich, M., A&A 401, 73 (2003)

[Wolf et al. 2003b] Wolf, C., Wisotzki, L., Borch, A., Dye, S., Kleinheinrich, M., Meisenheimer, K., A & A 408, 499-514 (2003)

[Wolf et al. 2004] Wolf, C., Meisenheimer, K., Kleinheinrich, M., Borch, A., Dye, S., Gray, M., Wisotzki, L., Bell, E.F., Rix, H.-W., Cimatti, A., Hasinger, G., Szokoly, G., A&A, accepted, astro-ph/0403666

Danksagung

An dieser Stelle möchte ich mich bei verschiedenen Menschen bedanken.

- Herrn Meisenheimer für die Betreuung meiner Arbeit und die Geduld, die er mit mir hatte.

- Christian Wolf und Herrn Rix für die Mitbetreuung meiner Arbeit.

- Herrn Appenzeller für die Erstellung des Zweitgutachtens.

- Rachel Somerville and Carlton Baugh for providing me with the results of their semianalytic models.

- The COMBO-17 team and the GEMS team for many things I learned during the meetings and telecons.

- Eric Bell for fruitful discussions and advices.

- Herrn Rix für die LBT-Reise, die mir die Gelegenheit gegeben hat, einmal Teleskope zu sehen.

- Den Professoren, bei denen ich interessante Vorlesungen gehört habe.

- Sigfried Falter, Stefan Noll, Angela Hempel und Christan Tapken für das Korrekturlesen meiner Arbeit.

- Joana Costa für die gute Zusammenarbeit in unserem gemeinsamen Amt.

- Angela Hempel für manchen guten Rat.

- Christian Tapken für interessante Diskussionen zu astronomischen Themen.

- Robert Weiß für interessante Diskussionen zu anderen Themen.

- Anja Müller dafür, daß sie mir eine sehr gute Freundin ist.